minerals

MDPI

Article

Geochemistry of a Mafic Microgranular Enclave-Bearing Late Paleozoic Pluton: Insights from Major, Trace and Rare Earth Element Systematics of the Variscan Kastoria Intrusion (Northwest Greece)

Ioanna Gerontidou [1,*], Antonios Koroneos [1,*], Valentin Ganev [2], Lambrini Papadopoulou [1], Alexandros Chatzipetros [3] and Kyriaki Pipera [1]

[1] Department of Mineralogy-Petrology-Economic Geology, School of Geology, Aristotle University of Thessaloniki, 54124 Thessaloniki, Greece; lambrini@geo.auth.gr (L.P.); kpipera@geo.auth.gr (K.P.)
[2] Geological Institute, Bulgarian Academy of Sciences, 1113 Sofia, Bulgaria
[3] Department of Structural, Historical & Applied Geology, School of Geology, Aristotle University of Thessaloniki, 54124 Thessaloniki, Greece
* Correspondence: ioangero@geo.auth.gr (I.G.); koroneos@geo.auth.gr (A.K.)

Abstract

The Late Paleozoic Kastoria intrusion in NW Greece is an MME-bearing granitoid pluton emplaced within the Pelagonian Zone of the Internal Hellenides. This study integrates major-, trace-, and rare earth element geochemistry to evaluate relationships among the host granitoids (GR) and the mafic microgranular enclaves (MME), magma evolution, and tectonomagmatic affinity. The GR are high-K calc-alkaline and metaluminous to peraluminous rocks, whereas the MME are less evolved and predominantly metaluminous. Both lithologies show LREE and LILE enrichment with negative Nb–Ta–Ti anomalies, indicating shared subduction-related geochemical inheritance. The MME have higher total REE abundances and flatter HREE patterns than the GR. The geochemical data indicate open-system evolution involving mafic recharge, magma mingling, limited hybridization, felsic differentiation, and increasing amphibole- and accessory-phase control. The GR display a moderate high-Sr/Y affinity, but partly decoupled Sr/Y and REE criteria argue against a classical adakite interpretation. On the contrary they suggest a relatively deep, plagioclase-poor stage of magma source evolution. Th/Yb–Ba/La systematics further indicate a sediment-influenced, subduction-modified mafic source. The Kastoria pluton is interpreted as a composite high-K calc-alkaline I-type system emplaced during late/post-collisional Variscan reorganization, with its inherited arc-like signature and slab-failure affinity consistent with slab-related reorganization along the Palaeotethyan ocean closing.

Keywords: Kastoria pluton; mafic microgranular enclaves; I-type granitoids; high-K calc-alkaline magmatism; whole-rock geochemistry; Variscan magmatism

Academic Editors: Saumitra Misra and Chad D. Deering

Received: 25 September 2026
Revised: 24 October 2026
Accepted: 28 October 2026
Published: 29 October 2026

Copyright: © 2026 by the authors. Licensee MDPI, Basel, Switzerland. This article is an open access article distributed under the terms and conditions of the Creative Commons Attribution (CC BY) license.

1. Introduction

The Variscan orogeny represents a major event of Paleozoic crustal reworking and granitoid magmatism in Europe and the peri-Mediterranean region [1–3]. Carboniferous to Permian granitoids associated with this orogenic cycle, record magmatism generated during changing subduction, collisional, and late-orogenic conditions within the evolving

Variscan belt [1,3,4]. Remnants of this magmatic record are preserved within the crystalline basement complexes of the Hellenides, where subsequent Mesozoic–Cenozoic tectonometamorphic overprinting has complicated reconstruction of their original petrogenetic and tectonomagmatic evolution [5–8]. The petrogenesis and tectonomagmatic significance of the Hellenic Carboniferous to Permian granitoids remain less well constrained than those of equivalent suites in central and western Europe [9].

Mafic microgranular enclaves (MME) are particularly informative components of granitoid systems because they record the interaction between compositionally contrasting mafic and felsic magmas. Their occurrence may reflect injection of relatively mafic magma into a felsic magma reservoir, followed by variable degrees of magma mingling, chemical exchange, hybridization, and crystal transfer [10–13]. Consequently, integrated comparison of host granitoids and MME can provide constraints on magma recharge, differentiation, and the extent to which plutons evolved as open rather than closed magmatic systems. Such enclaves are widely reported in Variscan granitoid magmas, where they have been interpreted as evidence for magma mixing processes during Late Paleozoic crustal evolution [1,4,11].

The Pelagonian Zone of the Internal Hellenides provides a key record of this evolution, preserving a polyphase pre-Alpine basement affected by Paleozoic magmatism and later Alpine tectonometamorphic overprinting [6,14–16]. Although regional geological and geochronological studies have clarified parts of the Late Paleozoic magmatic framework, systematic whole-rock geochemical studies of individual plutons remain limited. Consequently, the magma sources, differentiation process, role of mafic–felsic interaction, and geodynamic affinities of many Pelagonian granitoids are still insufficiently constrained [5,8,17].

The Kastoria pluton of northwestern Greece is a Late Carboniferous granitoid intrusion in the Pelagonian basement and forms part of the Variscan magmatic record of the Internal Hellenides [8,14,18]. Previous studies have focused mainly on its regional geological setting [7], petrography, and mineralogical characteristics [18], including the magmatic to subsolidus evolution of its accessory mineral assemblages [19]. However, a comprehensive whole-rock geochemical investigation integrating major elements, trace elements, and REEs for both the host granitoids and associated enclaves has not yet been undertaken.

This study presents whole-rock major-, trace-, and rare earth element (REE) data for the host granitoids (GR) and associated mafic microgranular enclaves (MME) of the Kastoria pluton. The geochemical dataset is used to document compositional relationships between the two lithological groups and to discuss the magmatic evolution and tectonomagmatic affinities of this MME-bearing Late Paleozoic intrusion within the Pelagonian basement. The results contribute to new whole-rock geochemical constraints on the Kastoria pluton and its place within the broader Variscan magmatic record of the Internal Hellenides.

2. Geological Setting

The Pelagonian Zone is one of the main geotectonic zones of the Internal Hellenides. It is interpreted as a Gondwana-derived microcontinent that preserves a polymetamorphic pre-Alpine basement comprising gneisses, amphibolites, schists, and marbles, intruded by granitoids of Paleozoic to Mesozoic age [14,16]. This crystalline basement records a prolonged geological history, including a lowermost metasedimentary succession interpreted to be older than ca. 700 Ma and Ediacaran orthogneissic magmatism at ca. 600 Ma, followed by Variscan magmatic at ca. 300 Ma and metamorphic overprinting and later Alpine deformation and nappe stacking [5,8,14,15,20].

The Kastoria intrusion is situated northwest of the Pelagonian Zone (Figure 1) and has been dated first by Mountrakis [7] at 302.4 ± 5/15 Ma and most recently by Zlatkin et al. [8] at 300 ± 2 Ma, placing its crystallization within the Late Carboniferous (Variscan). The pluton is prominently exposed on Mt. Verno, where it intrudes the Paleozoic metasedimentary and metamorphic rocks of the Kleisoura Series [14]. Previous studies have established the general mineralogical characteristics of the Kastoria pluton [18], while more recent work has clarified the mineralogy and mineral chemistry of its accessory phases and documented the magmatic to subsolidus overprint affecting both host granitoids and enclaves [19].

The present structural configuration of the pluton is strongly controlled by Alpine tectonism. Mylonitization, foliation development, and local gneissification are particularly pronounced along the pluton margins, where primary magmatic fabrics are largely overprinted and many outcrops exhibit augen gneissic textures [19]. Tectonic contacts dominate at the pluton boundaries, and no contact metamorphic aureoles have been confirmed in recent field investigations, suggesting that earlier reported contact metamorphic assemblages [7] may reflect tectonic rather than magmatic thermal effects.

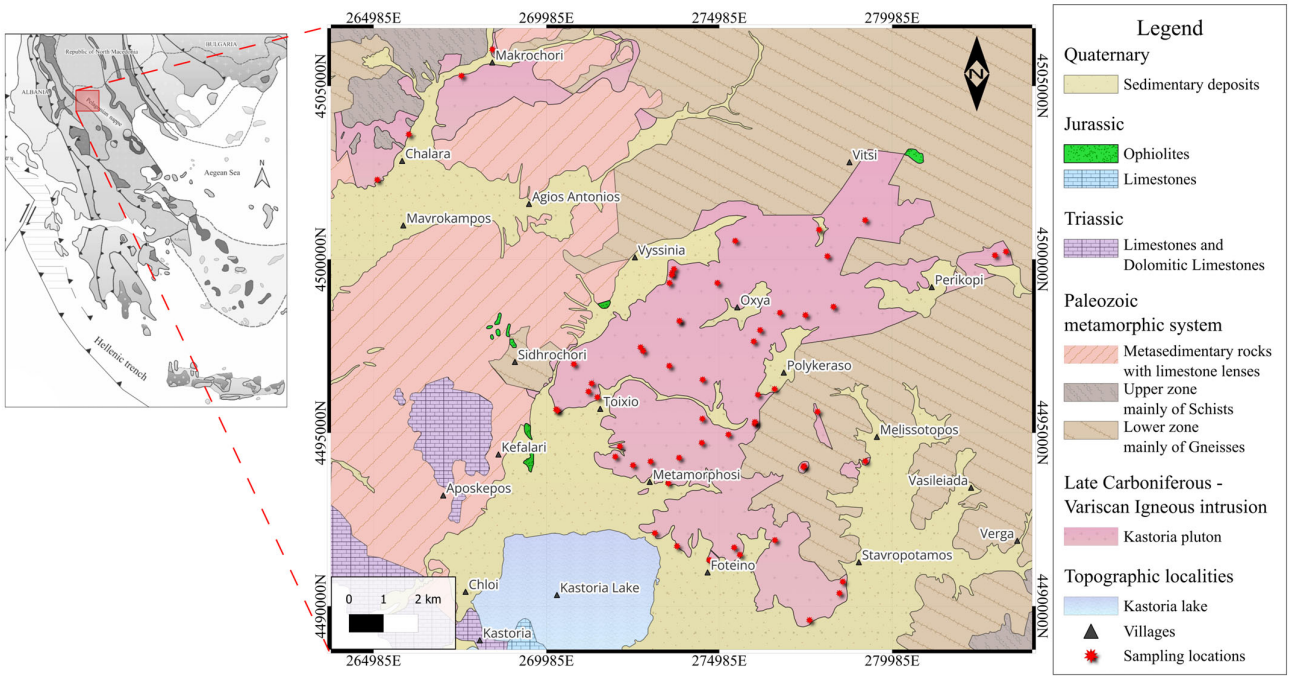


Figure 1. Petrographic map of the Kastoria pluton, reproduced and modified from Gerontidou et al. [19].

3. Materials and Methods

Fresh to minimally altered samples were preferentially selected during field sampling, and representative thin sections were examined under a polarizing microscope prior to geochemical interpretation to confirm lithological classification and to assess the degree of alteration, deformation, and secondary mineral replacement.

Whole-rock major elements and selected trace elements were determined with Wavelength-Dispersive X-ray Fluorescence (WD-XRF) on pressed powder pellets using the Supermini200 benchtop spectrometer (Rigaku Corporation, Tokyo, Japan) at Aristotle University of Thessaloniki, Greece. The instrument is equipped with a Pd-anode X-ray tube operated at 200 W, a Zr primary-beam filter, LiF(200) and PET analyzing crystals, and flow proportional (PC) and scintillation (SC) detectors. Measurements on the solid pellets

were made under vacuum, and data reduction was carried out using the ZSX Guidance software (Rigaku Corporation, Tokyo, Japan). Sample powders were mixed with Hoechst wax binder (CEREOX, FLUXANA GmbH & Co. KG, Bedburg-Hau, Germany) in a 4:1 sample:binder ratio, homogenized, and pressed into 40 mm diameter pellets following the protocol of [21]. Major elements were quantified as oxides (SiO_2, Al_2O_3, K_2O, Na_2O, MgO, CaO, TiO_2, MnO, Fe_2O_3, P_2O_5, SO_3) together with selected trace elements (Rb, Sr, Ba, Zr, V, Cr, Co, Ni, Cu, Zn, Pb, Sc, Y, Ga, and Nb). Loss on ignition (LOI) was determined by heating the dried sample powders at 1050 °C for two hours. LOI values were calculated from the weight difference before and after ignition. For the method calibration, 19 certified reference materials (CRMs from FLUXANA GmbH & Co. KG, Bedburg-Hau, Germany) were used, and analytical quality was monitored through drift correction (BR SQ1N and BR SQ3N glasses from Bruker Corporation, Billerica, MA, USA), check samples, and repeated analysis of standards. Full details of sample preparation, calibration strategy, matrix and overlap corrections, detection limits, and method validation are documented by Gerontidou and Koroneos [21]. The geochemical dataset used in this study comprises 63 whole-rock analyses from the Kastoria intrusion: 51 for the host granitoid and 12 for the enclaves.

The whole-rock trace element and rare earth element (REE) concentrations were determined for 20 samples with LA-ICP-MS technique at the Geological Institute, Bulgarian Academy of Sciences, Sofia, using the New Wave Research UP 193 nm excimer laser-ablation system coupled to a PerkinElmer ELAN DRC-e ICP-MS. Analyses were performed on fused glass beads prepared from powdered rock samples using a mixed lithium borate flux (66% $Li_2B_4O_7$ and 34% $LiBO_3$) at a sample-to-flux ratio of 1:8, with LiI added as a non-wetting agent. The resulting glass beads were mounted in epoxy resin and finely polished to obtain a flat analytical surface. During the sample introduction, optimal helium gas carrier flow in the laser ablation cell. Ablation was conducted using a 50 μm spot diameter, 95% laser energy, an energy density of 8.0–8.1 J cm^{-2}, and a repetition rate of 8 Hz. The ICP-MS was operated under dry-plasma conditions in standard mode, without collision gas in the dynamic reaction cell, using peak-hopping acquisition and dual-detector mode. Helium carrier gas was supplied at 0.92 L min^{-1}, whereas Ar nebulizer and auxiliary gas flows were set to 0.80 and 0.92 L min^{-1}, respectively; RF power was 1500 W. Oxide production was maintained below 0.5% ThO. Background and ablation-signal acquisition times were 40 and 50 s, respectively. A total of 34 masses were collected (Sc45, V51, Cr53, Co59, Ni62, Cu65, Zn66, Ga71, Rb85, Sr88, Y89, Zr90, Nb93, Cs133, Ba137, La139, Ce140, Pr141, Nd146, Sm147, Eu151, Gd157, Tb159, Dy163, Ho165, Er167, Tm169, Yb173, Lu175, Hf178, Ta181, Pb208, Th232, U238) with dwell times of 10 ms for trace elements and 20 ms for REE. Three spots per sample were analyzed, and the mean value was used for interpretation. Quantification was carried out using Ca (^{42}Ca signal) and Si (^{29}Si signal) concentrations previously determined by WD-XRF as internal standards, with Ca serving as the primary internal standard and Si as a secondary check to monitor matrix consistency. As external calibration standards, the synthetic glasses NIST-610 and NIST-612 were used and measured approximately every 10 spots. Data reduction and element content calculations were performed with the SILLS software package (version 1.1.0, ETH Zurich, Zurich, Switzerland) [22].

4. Results

4.1. Petrology

The Kastoria intrusion is composed of porphyritic granitoids that host mafic enclaves. The host granitoid rocks (Figure 2) are characterized by a medium- to coarse-grained inequigranular fabric, in which K-feldspar megacrysts of perthitic microcline, are set in a matrix of quartz, plagioclase, biotite, and hornblende.



Figure 2. Representative macroscopic photographs of the host granitoid from the Kastoria pluton. (**a**) Field view of the host granitoid. (**b1**,**b2**) Close-up views showing the coarse, K-feldspar megacryst-bearing granitoid; (**b2**) highlights a ~5cm K-feldspar megacryst. (**c1**,**c2**) Hand specimens of the granitoid.

Plagioclase is subhedral and commonly altered to fine white mica (sericite) and epidote-group minerals (saussurite). Biotite occurs as brown to greenish and commonly shows partial discoloration and alteration. Hornblende is preserved in the less altered samples, whereas actinolite and chlorite occur as replacement products. Accessory phases include epidote, titanite, allanite, apatite, zircon, and magnetite. Microcline occur both as megacrysts and as matrix grains. Detailed petrographic micrographs and mineral-chemical textures are documented by Gerontidou et al. [19].

The enclaves are darker and finer-grained than the host rocks. They contain the same primary mineral assemblage as the granitoid rocks but differ in modal proportions, being richer in plagioclase, amphibole, and biotite and poorer in quartz and microcline. Secondary minerals of white mica, epidote, chlorite, actinolite, and calcite are common alteration products in both the host rocks and the enclaves. Despite variable degrees of secondary mineral replacement, the rocks preserve their primary magmatic mineral features and textural characteristics, allowing reliable lithological classification and interpretation.

The enclaves range from a few centimeters (Figure 3b) to several tens of centimeters in their longest dimension and commonly display lobate to crenulated contacts against the host rocks. The largest observed enclave (MET-11E) is approximately 30 cm in their longest dimension (Figure 3a), which is also the most coarse-grained among the enclaves documented.

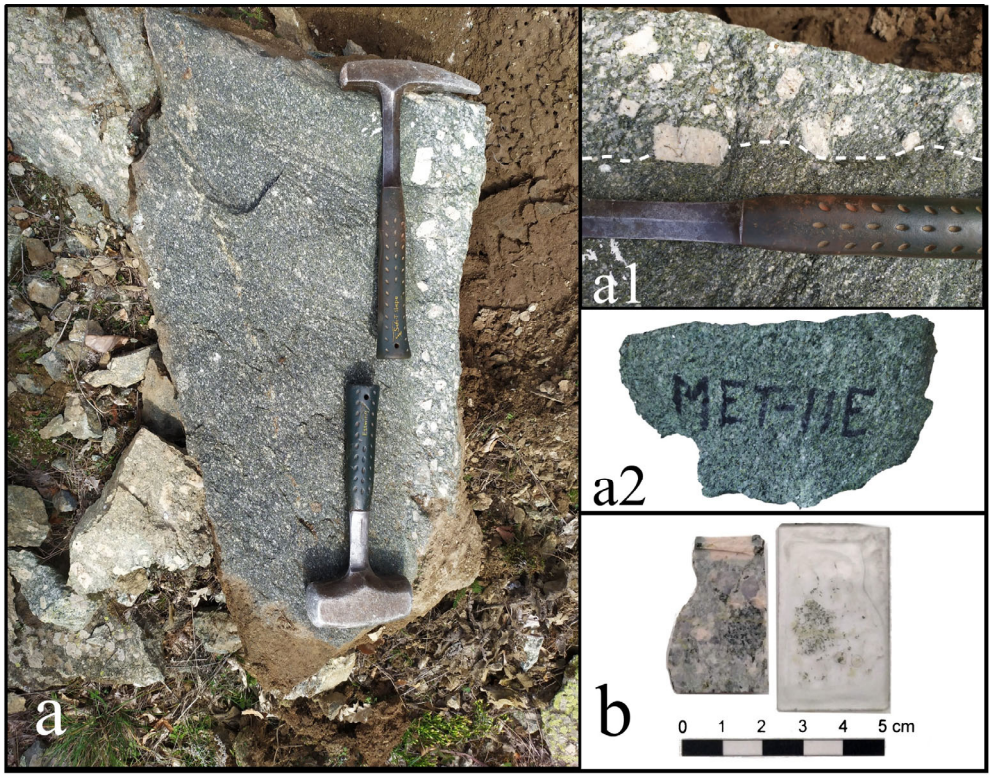


Figure 3. Representative macroscopic photographs of the enclaves from the Kastoria pluton. (**a**) Field view of the largest observed enclave (MET-11E) within the host granitoid. (**a1**) Close-up view showing the enclave-host contact, sharing host-derived K-feldspar megacryst. (**a2**) Hand specimen of the MET-11E enclave from (**a**). (**b**) Thin section of host granitoid enclosing a small enclave, distinguished by its darker color and finer grain size.

The Q–A–P classification diagram (Figure 4) illustrates the compositional distinction between the Kastoria host granitoids and the enclaves. Most granitoid samples plot within the monzogranite field, with minor extension toward granodiorite and quartz monzonite fields. The enclaves plot mainly within the quartz monzonite and monzonite, with a few samples extending toward the quartz monzodiorite field.

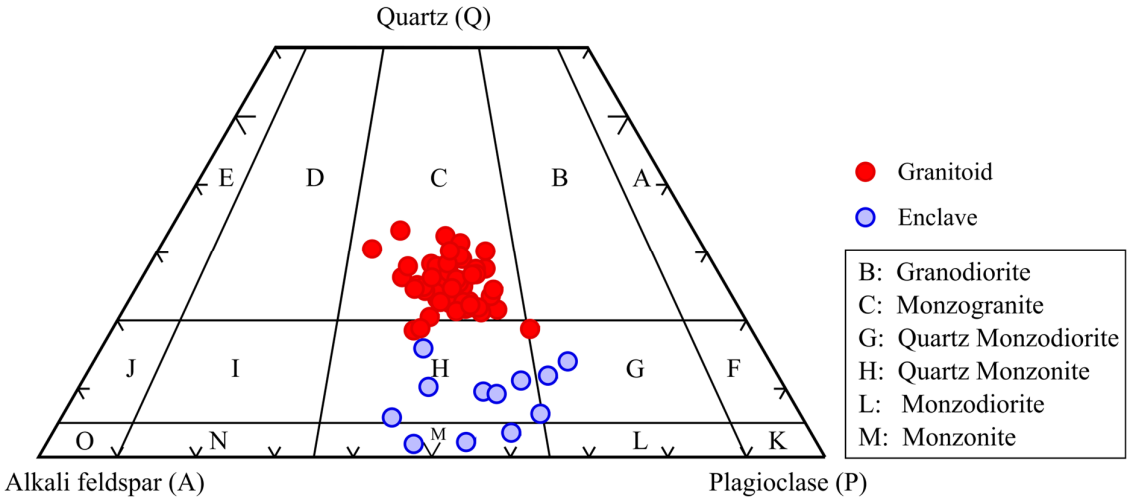


Figure 4. Normative Q–A–P classification diagram for the Kastoria host granitoids and enclaves (modified after Streckeisen [23]).

The Q-ANOR diagram (Figure 5) shows a clear compositional distinction between the Kastoria host granitoids and the enclaves. The host granitoids cluster mainly within the granite field, particularly within the syenogranite–monzogranite field, whereas the enclaves plot largely in the quartz monzonite to monzonite fields. The samples appear to define an array broadly parallel to the AC trend, indicating an alkali-calcic compositional affinity.

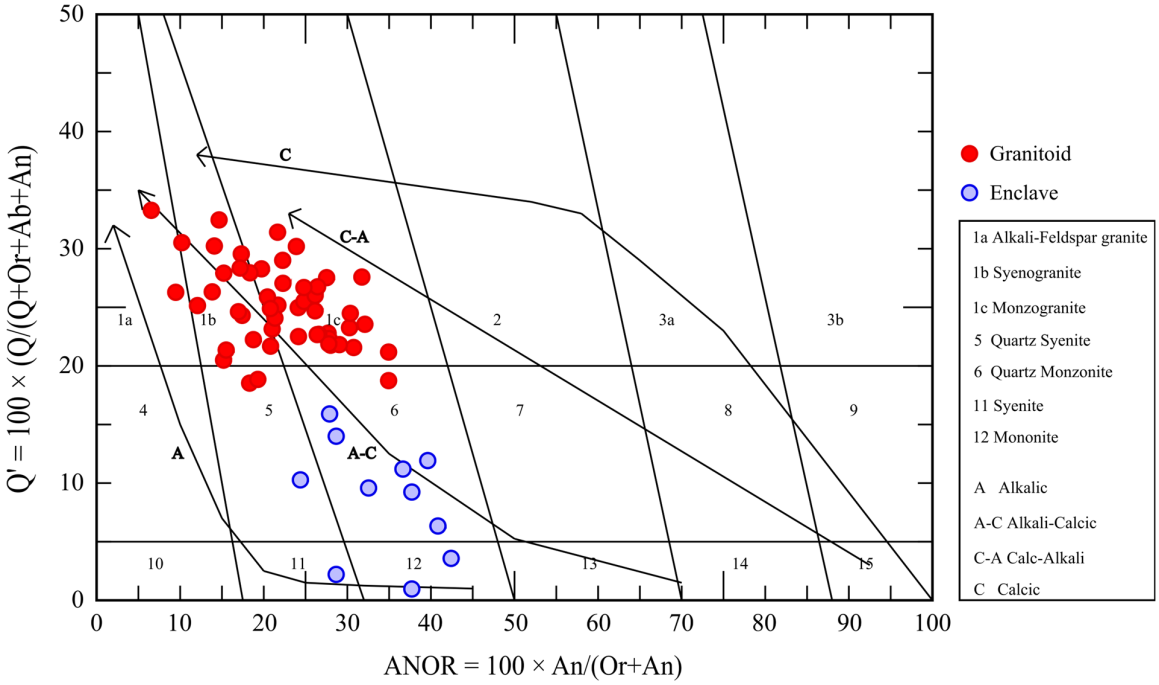


Figure 5. Modified Q-ANOR classification diagram for the Kastoria host granitoids and enclaves (modified after Whalen and Frost [24]).

On this basis, the host granitoids are hereafter referred to as GR, including the samples of monzogranitic to granodioritic composition, whereas the enclave suite is referred to as MME (mafic microgranular enclaves), comprising monzonitic to quartz monzonitic compositions. This designation reflects their darker color, finer-grained microgranular texture, and occurrence as magmatic enclaves within the GR with sharing minerals along their margins.

4.2. Major and Trace Element Geochemistry

Major- and trace-element data for the GR and MME are reported in File S1. The SiO_2 content of GR ranges from 62.73 to 72.55 wt.% SiO_2 (mean 66.76 wt.%), whereas in the MME range from 49.38 to 60.51 wt.% SiO_2 (mean 56.25 wt.%). Relative to the GR, the MME are enriched in MgO (2.92–7.91 wt.% versus 0.38–2.48 wt.%), CaO (3.10–8.04 wt.% versus 0.65–3.59 wt.%), TiO_2 (0.61–1.33 wt.% versus 0.13–0.56 wt.%), and Fe_2O_3 (6.65–11.25 wt.% versus 1.32–4.43 wt.%).

In the AFM diagram (Figure 6a), both GR and MME define a calc-alkaline array, with the MME extending toward more Fe–Mg-rich compositions. In the K_2O versus SiO_2 diagram (Figure 6b), both lithologies plot predominantly within the high-K calc-alkaline field and toward the shoshonitic field. In the modified alkali-lime index diagram (MALI) the GR plot mainly within the alkali-calcic field, whereas the MME show a broader distribution, ranging from calc-alkalic to alkalic compositions (Figure 6c).

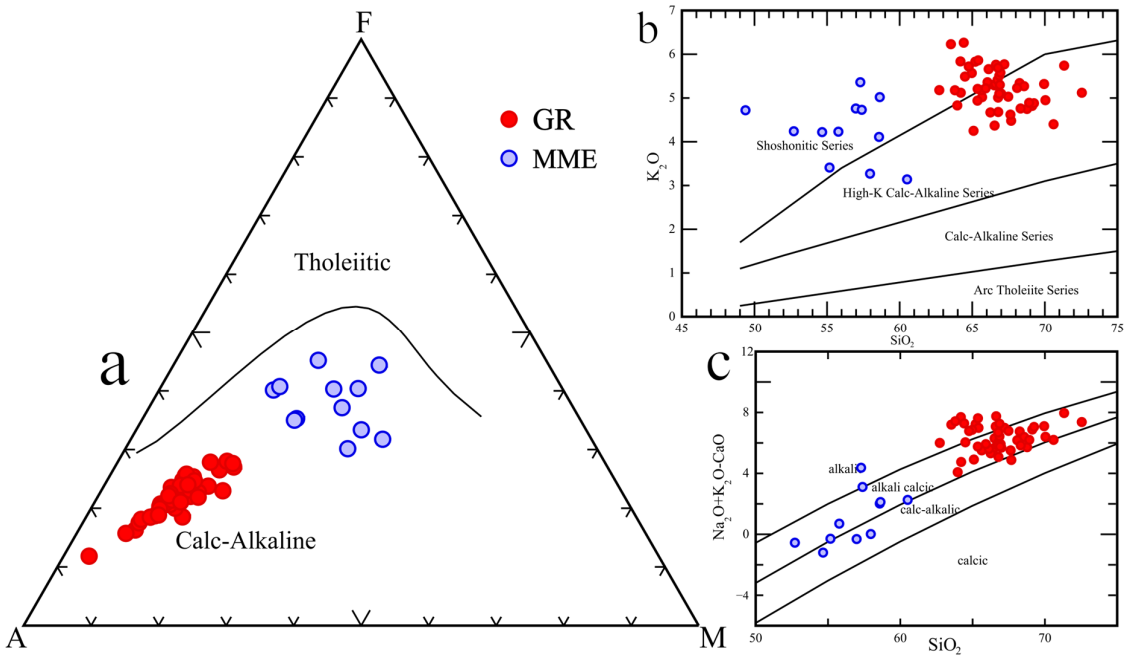


Figure 6. Magma-series geochemical classification diagrams for the Kastoria pluton. (**a**) AFM diagram (modified after Irvine and Baragar [25]). (**b**) K_2O versus SiO_2 diagram (modified after Peccerillo and Taylor [26]). (**c**) Modified alkali–lime index $Na_2O + K_2O - CaO$ versus SiO_2 (MALI) (modified after Frost et al. [27]).

Alumina saturation indices distinguish GR from the MME. The GR range from metaluminous to peraluminous compositions (A/CNK = 0.92–1.44; mean = 1.12), whereas the MME are predominantly metaluminous (A/CNK = 0.43–1.12; mean = 0.70). In the A/NK versus A/CNK diagram (Figure 7a), the GR span along the metaluminous–peraluminous boundary, whereas the MME plot mainly at lower A/CNK values within the metaluminous field. The A/CNK versus SiO_2 (Figure 7b) and A/CNK versus $Fe_2O_3 + MgO$ (Figure 7c) diagrams show that the GR form a comparatively restricted population at lower $Fe_2O_3 + MgO$ contents and generally higher A/CNK values, whereas the MME extend toward higher $Fe_2O_3 + MgO$ contents and lower A/CNK values.

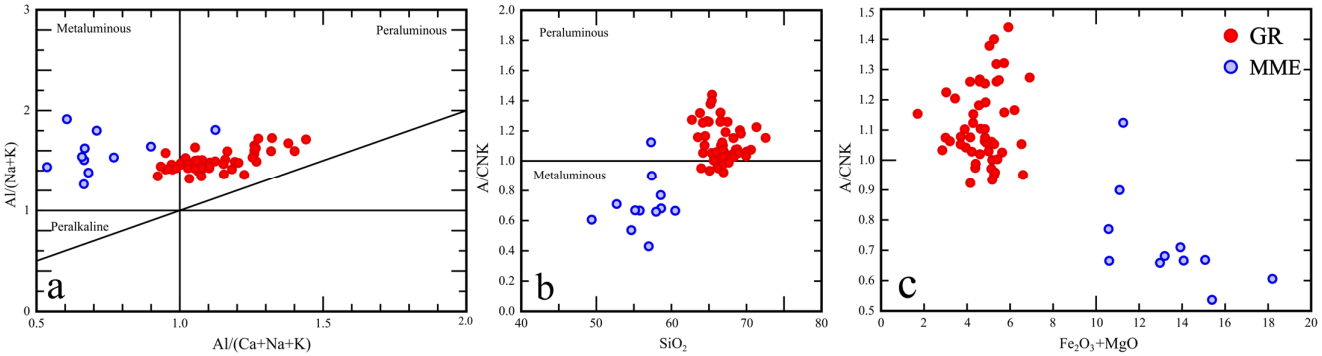


Figure 7. Variation of Alumina Saturation Index of the Kastoria pluton. (**a**) A/NK versus A/CNK diagram (modified after Maniar and Piccoli [28]). (**b**) A/CNK versus SiO_2 diagram (modified after Shand [29]). (**c**) A/CNK versus $Fe_2O_3 + MgO$ diagram.

The Harker-type variation diagrams show the major-element variation against SiO_2 for the GR and the MME (Figure 8). The MME occupy the lower-SiO_2, more mafic part of the compositional array and are characterized by higher Fe_2O_3, TiO_2, MnO, CaO, MgO,

and P_2O_5 contents relative to the GR. In contrast, the GR occupy the more silica-rich part of the array and generally display lower concentrations of the mentioned oxides.

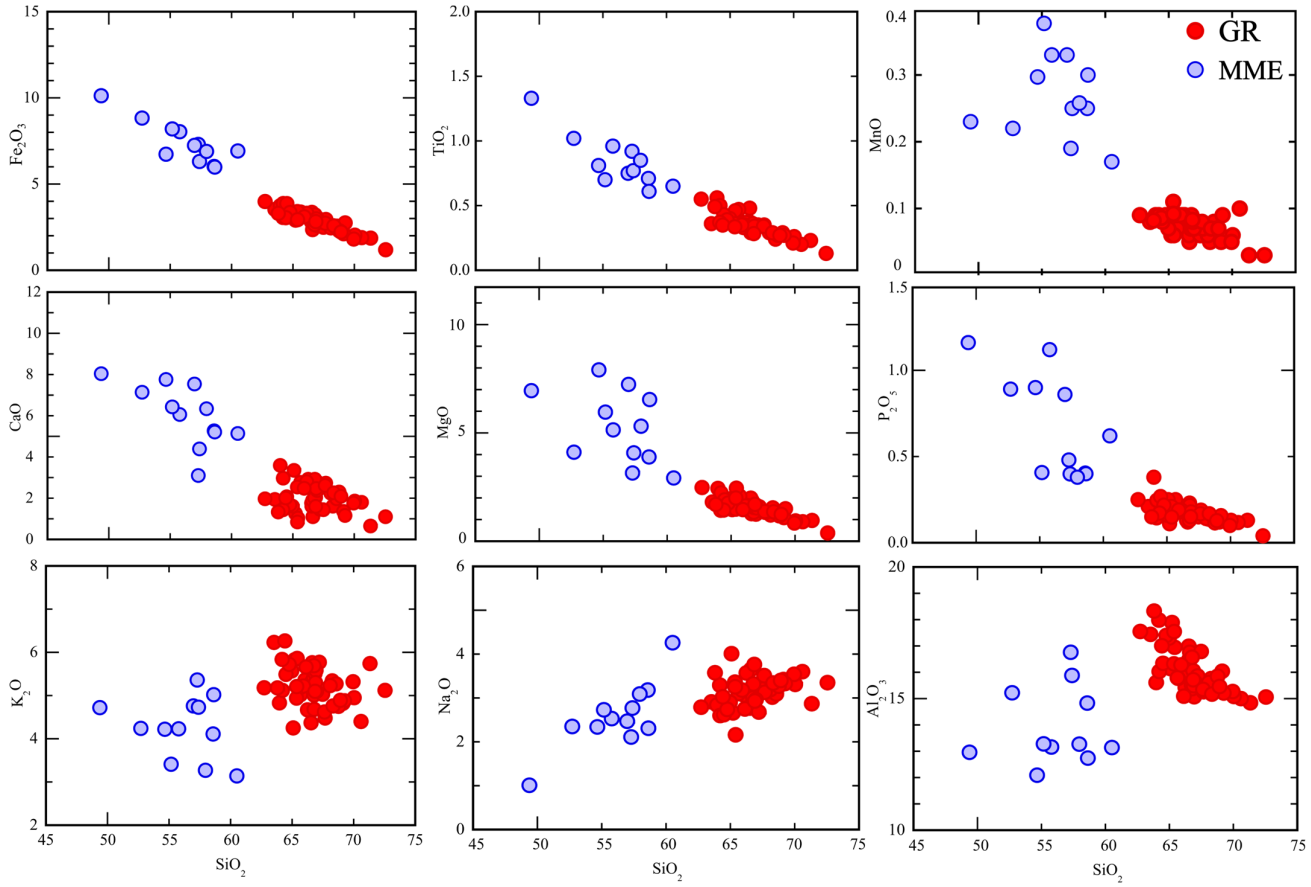


Figure 8. Harker-type variation diagrams for selected major elements against SiO_2 for the Kastoria pluton.

Across the combined dataset, Fe_2O_3, TiO_2, MnO, CaO, MgO, and P_2O_5 broadly decrease with increasing SiO_2, whereas K_2O and Na_2O are more scattered but tend to be higher in the GR than in the MME. Al_2O_3 displays a less systematic behavior: it decreases overall within the GR population, but in the MME it forms a scattered field with, at most, a weak positive tendency toward higher SiO_2.

The trace-element Harker-type diagrams show a respective compositional separation between the GR and MME (Figure 9). The MME at the lower-SiO_2 range, generally display higher V, Cr, Ni, Sc, Y, and Zr concentrations than the GR. In contrast, Rb values overlap substantially between the two groups, whereas Sr and Ba are comparatively high in both lithologies but show broad scatter, particularly among the MME. Across the combined dataset, V, Cr, Ni, Sc, Y, and, more broadly, Zr decrease with increasing SiO_2, whereas Ba, Sr, and Rb show more dispersed distributions without consistent linear trends. The clearer behavior of V, Cr, Ni, and Sc relative to the large-ion lithophile elements (LILE) is consistent with stronger mineralogical control on these elements during compositional evolution [30].

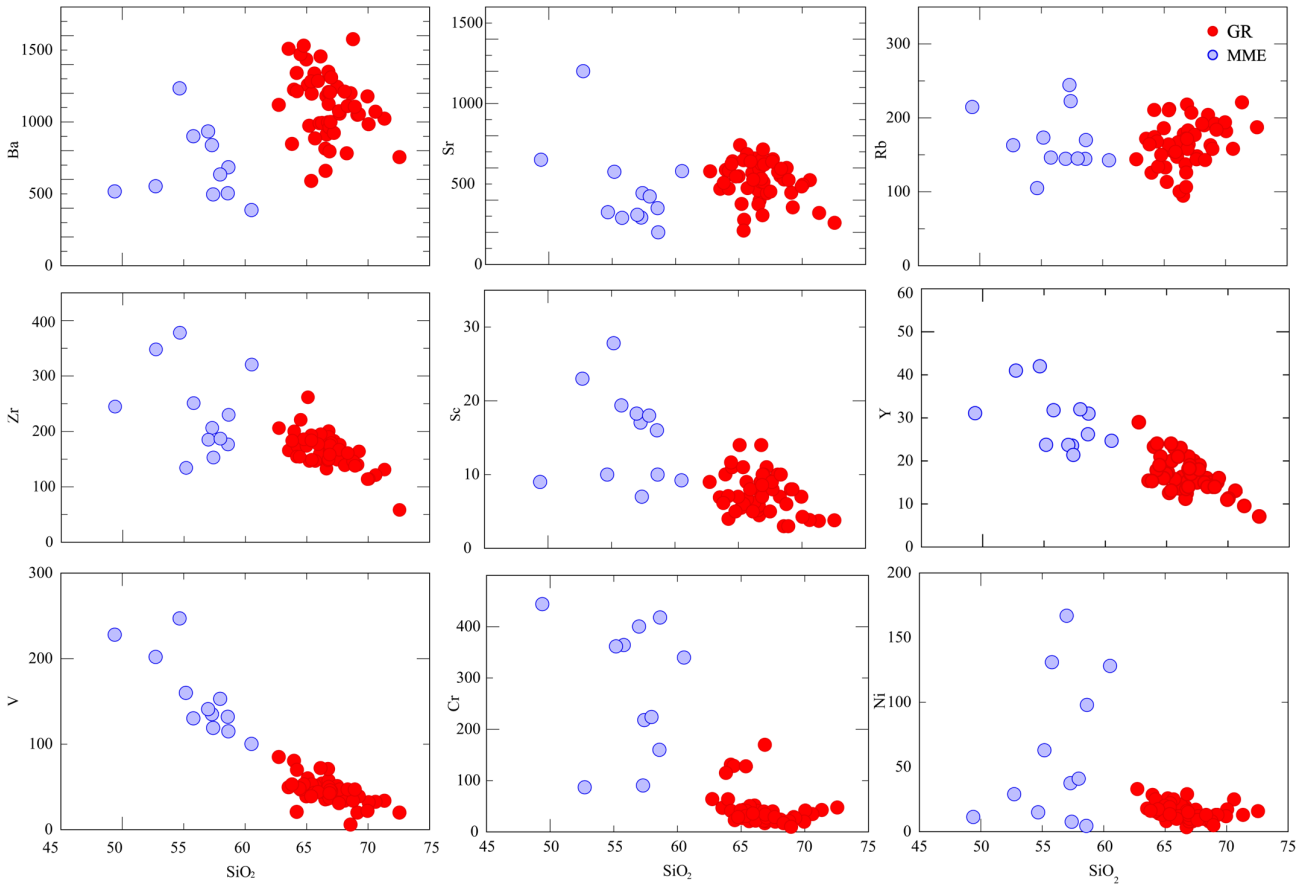


Figure 9. Harker variation diagrams for selected trace elements against SiO_2 for the Kastoria pluton.

Overall, the major- and trace-element systematics define a broad compositional contrast between the GR and MME. The GR occupy the higher-SiO_2 portion of the dataset and show decreasing Fe_2O_3, MgO, CaO, TiO_2, and P_2O_5 contents with increasing SiO_2. Al_2O_3 also decreases overall within the GR population, whereas K_2O and Na_2O show greater scatter. The MME occur at lower SiO_2 content and display systematically higher Fe_2O_3, MgO, CaO, TiO_2, and P_2O_5 contents, together with elevated V, Cr, Ni, Sc, Y, and Zr concentrations. Al_2O_3 show a slight positive trend within the MME. LILE elements like Ba, Sr, and Rb show partial overlap between the two groups and more dispersed behavior than the compatible elements. Although several elements covary with SiO_2, the GR and MME form offset fields rather than a single continuous array, suggesting that the MME represent a distinct, less differentiated component of the same plutonic system [12,30,31].

4.3. REE Systematics

Chondrite-normalized REE patterns show that both GR and MME are strongly enriched in LREE relative to HREE and define broadly subparallel trends (Figure 10a). The MME are systematically shifted to higher absolute REE abundances than the GR and display slightly flatter HREE patterns. Despite these higher absolute values, the MME patterns define a comparatively narrower shaded section, particularly from the MREE to HREE range. Both groups show modest to no negative Eu anomalies on average, whereas no systematic Ce anomaly is evident. For the GR, mean Eu/Eu* is 0.90 (range 0.73–1.12) and for the MME is 0.86 (range 0.65–1.12), broadly resembling the GR values. The mean $(La/Yb)_N$ of the MME is 11.9 (range 6.5–17.8), lower than the 14.9 of the GR (range 8.3–21.4). Although the two groups partly overlap, the lower $(La/Yb)_N$ average of the MME indicates slightly flatter REE patterns and weaker LREE/HREE fractionation relative to

the GR. On the contrary, the higher average $(La/Yb)_N$ of the GR reflects steeper REE profiles and stronger relative enrichment of LREE over HREE.

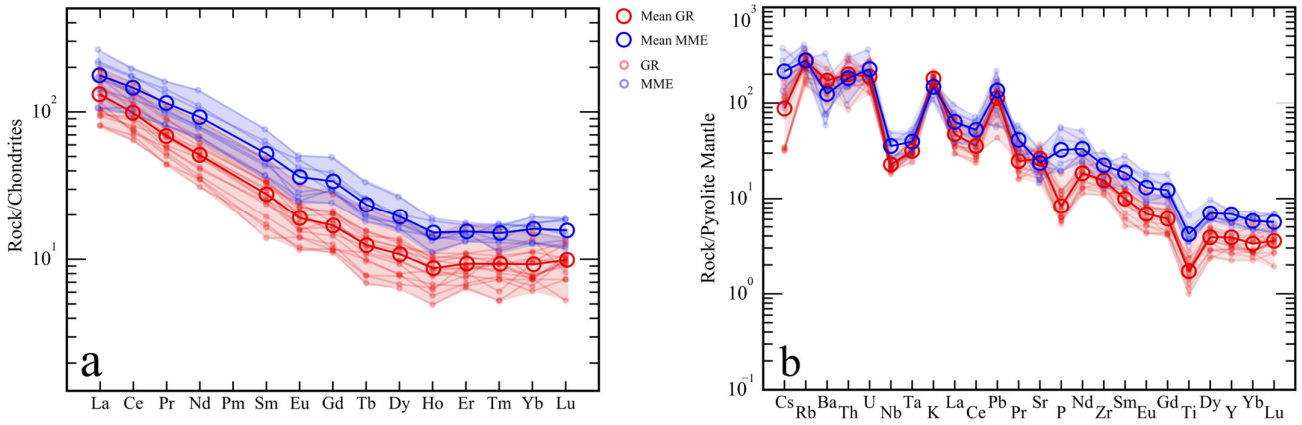


Figure 10. Spider diagrams for the Kastoria pluton. (**a**) Chondrite-normalized REE patterns. (**b**) Primitive mantle-normalized multi-element patterns. Normalization values from Sun and McDonough [32]. Shaded fields represent the compositional range of each group; bold open symbols indicate group means.

Primitive mantle-normalized multi-element patterns of the GR and MME are presented in Figure 10b. Both groups display broadly similar patterns, characterized by enrichment in LILE relative to high-field-strength elements (HFSE) and Pb together with negative Nb, Ta, and Ti anomalies. A positive Pb anomaly is evident in both lithological groups, whereas the negative P anomaly is more distinct in the GR. P anomaly for the MME ranges from 0.74 to 2.27 with mean 1.26 and for the GR it ranges from 0.25 to 0.61 with mean 0.40. Relative to the GR, the MME generally show higher abundances of several incompatible elements, including REE, Y, and Zr, but preserve a comparable overall multi-element pattern.

4.4. Tectonic Setting Discrimination

Trace-element discrimination diagrams for the Kastoria pluton are shown in Figure 11. In the Rb versus (Yb + Ta) and Ta versus Yb diagrams (Figure 11a,c), both GR and MME plot in the VAG (volcanic arc granite) field of Pearce et al. [33], slightly extending toward the syn-COLG (syn-collisional granite) field; moreover, in the updated scheme of Whalen and Hildebrand [34], they fall within the slab-failure field. The MME generally plot at higher Yb + Ta, Yb, and Ta values than the GR, although the two groups partly overlap. No samples plot within the arc or A-type fields in these diagrams.

In the Rb versus (Y + Nb) and Nb versus Y diagrams (Figure 11b,d), both lithological groups plot within the volcanic-arc granite (VAG) and syn-collisional field (syn-COLG), extending to within-plate granite (WPG) fields of Pearce et al. [33]. When applying the updated boundaries of Chen et al. [35], shown by the green shaded fields, the classification is broadened and all samples plot exclusively within the convergent margin granitoid (CMG) field. The GR form a relatively compact cluster, whereas the MME extend toward higher Y + Nb, Y, and Nb values. In the Th/Ta versus Yb diagram (Figure 11e), all samples plot within the active continental margin field. The GR extend to higher Th/Ta values, whereas the MME define a broader range toward higher Yb values.

Overall, the discrimination diagrams consistently place the Kastoria pluton within convergent-margin to collisional fields across volcanic-arc, active continental margin, and slab-failure fields [33,34,36].

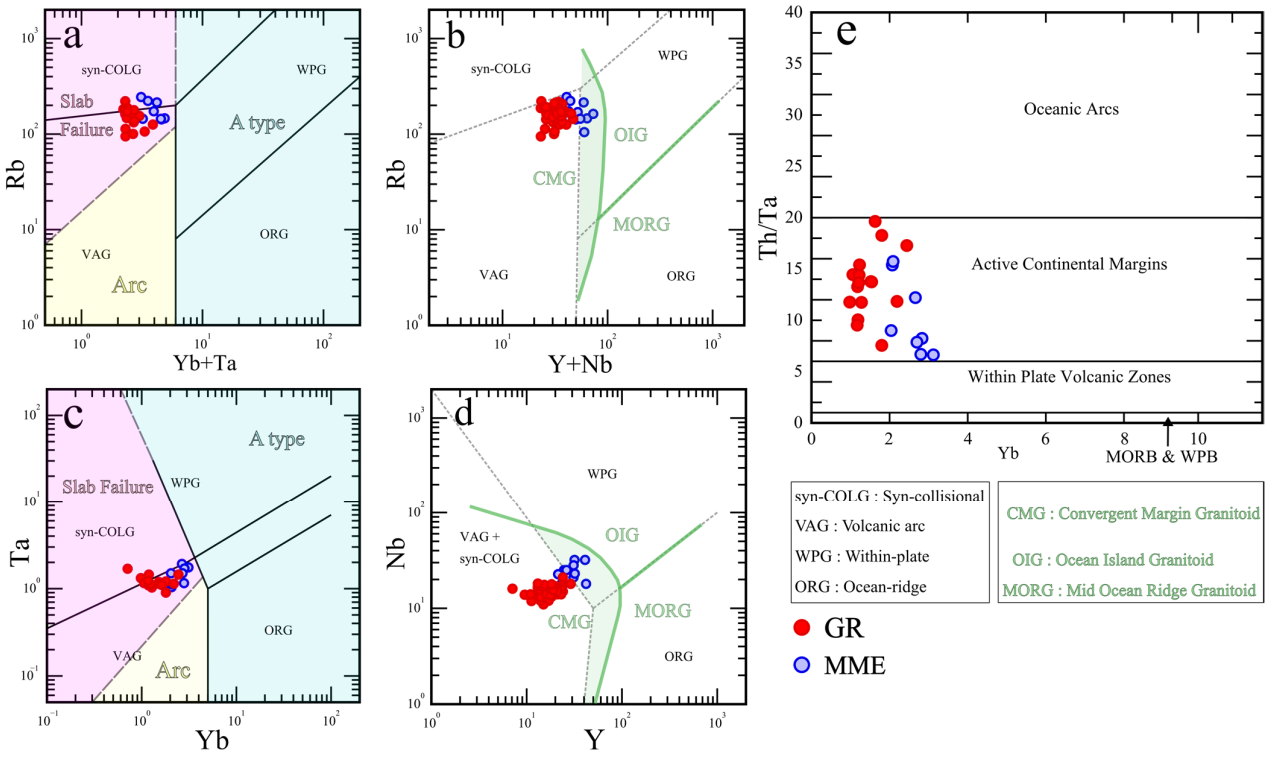


Figure 11. Trace-element tectonomagmatic discrimination diagrams for the Kastoria pluton. (**a**) Rb versus (Yb + Ta). (**b**) Rb versus (Y + Nb). (**c**) Ta versus Yb. (**d**) Nb versus Y diagrams. (**a**–**d**) Modified after Pearce et al. [33]. Arc, slab-failure, and A-type subdivisions in diagrams (**a**,**c**) are after Whalen and Hildebrand [34]. Green boundaries with CMG, OIG and MORG in diagrams (**b**,**d**) are after Chen et al. [35]. (**e**) Th/Ta versus Yb diagram (modified after Gorton and Schandl [36]).

The additional discrimination diagrams shown in Figure 12 place the Kastoria intrusion mainly within arc- to collisional and late-orogenic compositional fields.

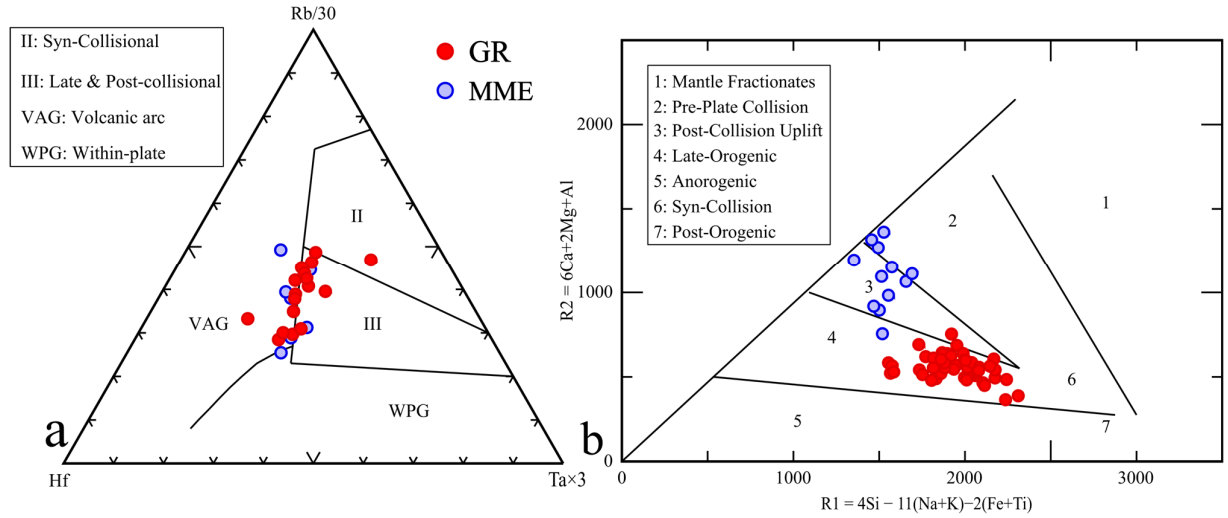


Figure 12. Tectonomagmatic discrimination diagrams for the Kastoria pluton. (**a**) Rb/30–Hf–Ta*3 ternary diagram (modified after Harris et al. [37]). (**b**) R1-R2 diagram [R2 = 6 × Ca – 2 × Mg + Al versus R1 = 4 × Si − 11(Na + K) − 2(Fe + Ti)] (modified after Batchelor and Bowden [38]).

In the Rb/30–Hf–Ta*3 ternary diagram (Figure 12a), both GR and MME plot close to the boundary between the volcanic-arc (VAG) and late & post-collisional fields [37] with

substantial overlap between the two groups. The R1–R2 diagram (Figure 12b) shows a clearer separation between the two groups. The GR plot primarily within the late-orogenic field, with several samples approaching the syn-collision field. In contrast, the MME plot mainly within the post-collision uplift field [38].

Together, these diagrams indicate that the Kastoria pluton extends to volcanic-arc, collisional, and late-orogenic compositional fields [37,38]. The GR plot mainly within the syn-collisional to late-orogenic fields, whereas the MME are predominantly displaced toward the post-collisional uplift field.

The trace-element discrimination diagrams of Whalen and Hildebrand [34] are shown in Figure 13. Following the compositional filters proposed by the authors, only samples with 55–70 wt.% SiO_2 and ASI < 1.1 were considered.

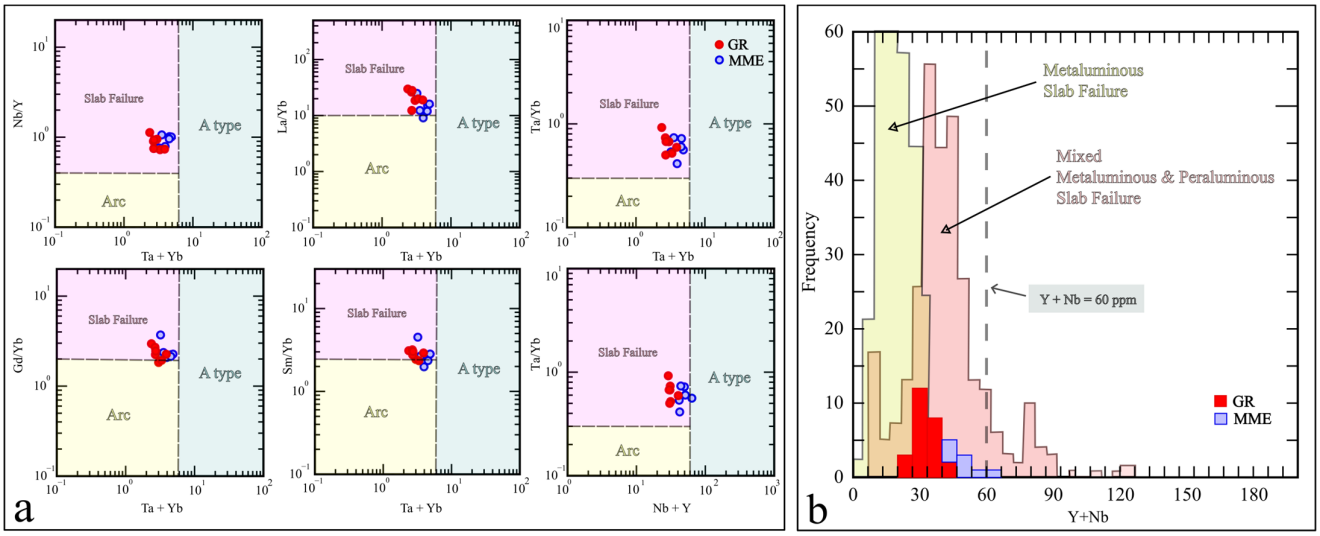


Figure 13. (**a**) Trace-element discrimination diagrams Arc, Slab Failure, A-type for the Kastoria pluton (modified after Whalen and Hilderbrand [34]). (**b**) Histogram of Y + Nb values for the Kastoria pluton; shaded fields defined by Whalen and Hildebrand [34].

The GR and MME plot predominantly within the slab-failure fields, forming very close clusters (Figure 13a). A small number of samples occur close to, or locally overlap, the arc–slab-failure boundary, particularly in the Ta/Yb diagrams, where slight dispersion toward lower Sm/Yb and La/Yb ratios are observed. This distribution reflects minor variability within the dataset but does not disrupt the overall data clustering of the samples within the slab-failure fields.

The Y + Nb histogram (Figure 13b) further supports this interpretation, showing that all selected samples have values below 60 ppm, the threshold used to distinguish arc and slab-failure granitoids from A-type. The data define a relatively narrow range, with most samples clustering toward the lower end of the distribution, reinforcing their affinity with slab-failure granitoids. Their distributions overlap the Y + Nb ranges of the metalluminous and mixed metalluminous–peraluminous slab-failure reference populations of [34]. This comparison is consistent with the alumina-saturation relations shown in Figure 7, where the GR span metaluminous to peraluminous compositions, whereas the MME are predominantly metaluminous.

Collectively, Figure 13 illustrates a consistent geochemical signature across multiple discrimination parameters, supporting a slab-failure affinity while highlighting limited internal variability within the Kastoria pluton.

4.5. Source- and Pressure-Sensitive Trace Element Systematics

To further evaluate trace-element variability of the Kastoria pluton in terms of its internal compositional differentiation and its sensitivity to source characteristics and pressure-dependent fractionation processes, Y-Sr/Y, Yb_{CN}-$(La/Yb)_{CN}$, and Ba/La-Th/Yb systematics are examined in Figure 14. These diagrams are commonly used to evaluate variations in Sr–Y and REE fractionation and to compare the relative behavior of fluid-mobile and incompatible trace elements in arc-related magmatic suites [39–42].

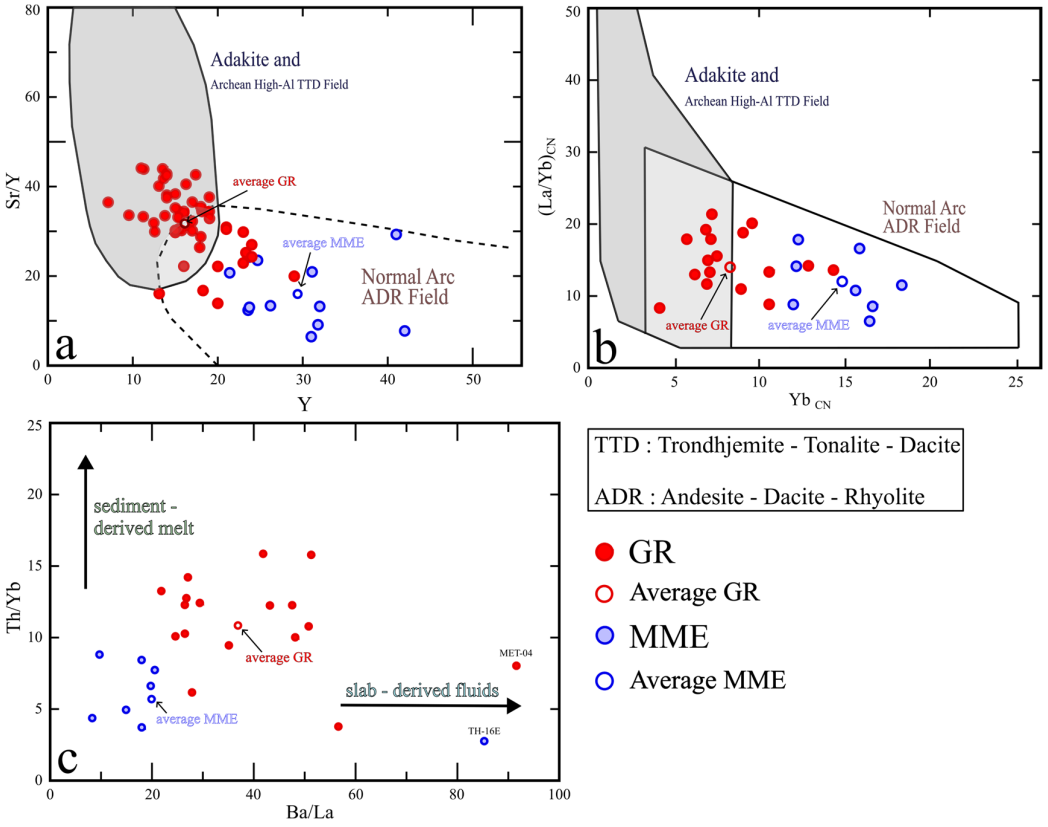


Figure 14. Source and pressure sensitive trace-element diagrams for the Kastoria pluton. (**a**) Sr/Y versus Y. (**b**) $(La/Yb)_{CN}$ versus Yb_{CN} (chondrite-normalized after [32]). (**a**,**b**) Modified after Defant et al. [39] and Martin [40]. (**c**) Th/Yb versus Ba/La diagram (modified after Woodhead et al. [41]).

The Sr/Y versus Y diagram shows a partial compositional offset between the GR and MME samples (Figure 14a). The GR generally show lower Y contents and higher Sr/Y ratios than the MME, with several samples overlapping or approaching the Adakite–Archean high-Al trondhjemite–tonalite–dacite (TTD) reference field. However, this overlap is not sufficient to classify the Kastoria granitoids as adakitic, because part of the GR population remains within the normal arc andesite–dacite–rhyolite (ADR) field and because Y-Sr/Y systematics may also be influenced by amphibole, titanite, allanite and apatite fractionation in evolved granitoid magmas [42]. In contrast, the MME plot predominantly within the normal arc ADR field and extend toward higher Y and lower Sr/Y values. The average GR composition is therefore displaced toward higher Sr/Y and lower Y relative to the average MME composition, indicating stronger Sr–Y fractionation in the granitoid host rather than a uniquely adakitic affinity [42–46].

The chondrite-normalized $(La/Yb)_{CN}$ versus Yb_{CN} diagram shows a related but less pronounced separation between the two lithological groups (Figure 14b). The GR generally plot at lower Yb_{CN} values and extend toward higher $(La/Yb)_{CN}$ ratios, whereas the MME extend toward higher Yb_{CN} and somewhat lower $(La/Yb)_{CN}$ values. The group

averages preserve this offset, consistent with the stronger average LREE/HREE fractionation observed in the GR REE patterns (Figure 10a). In contrast to the Sr/Y versus Y diagram, however, both groups plot predominantly within the overlap of the "Normal Arc Andesite–Dacite–Rhyolite (ADR)" field, and no clear population occupies strictly the Adakite field [32,40,42].

Th/Yb emphasizes variations in Th relative to the HREE, whereas Ba/La highlights relative enrichment of the fluid-mobile element Ba and has been widely applied to the comparison of subduction-related enrichment trends [41]. The MME form a comparatively compact field at lower Th/Yb and Ba/La values. Because the MME are compositionally less evolved than the granitoid host, they may preserve a closer record of mafic input to the system, prior to extensive felsic differentiation, whereas the GR are included to illustrate the compositional evolution and relationships between the mafic and felsic components of the pluton. A similar comparative approach, in which host granitoids and associated mafic enclaves are plotted together to evaluate source-related contrasts and magmatic evolution, has been applied to other enclave-bearing granitoid systems [47,48]. The average GR composition consequently occurs at higher Th/Yb and Ba/La than the average MME composition, although substantial overlap occurs between the two groups [41,49].

Two samples show particularly high Ba/La values relative to the main population, but for different compositional reasons (Figure 14c). MET-04, the most silica-rich (72.55 wt.%) evolved GR sample, has the highest Ba/La ratio among the analyzed granitoids (91.6). This is because of its very low La concentration (8.25 ppm) rather than high Ba (756 ppm). The low La content is accompanied by comparatively low ΣREE, Th, Y, Zr, Hf, and P_2O_5 abundances, which may indicate that the system reached saturation in accessory minerals, leading to strong depletion of these incompatible elements. Thus, the high Ba/La value of MET-04 is not interpreted as a Ba-enrichment from slab-derived fluids. In contrast, TH-16E represents a Ba-rich MME end member, with Ba/La of 85.3 resulting from its high Ba concentration (2166 ppm), whereas La (25.4 ppm) remains within the range of the MME population. TH-16E also has comparatively low Th/Yb (2.8), associated with relatively low Th and the generally higher Yb concentrations of the MME. Consequently, TH-16E should be treated as a local Ba-rich MME end member rather than as evidence for a suite-wide fluid-enrichment trend. Therefore, the high Ba/La values of MET-04 and TH-16E should not be interpreted as evidence for a single enrichment process; they instead demonstrate that similar ratio values may result from contrasting elemental controls.

5. Discussion

5.1. Nature of the Enclave-Host Association

The Kastoria pluton records the coexistence of a felsic granitoid host and a darker, finer-grained mafic microgranular enclave (MME) population that is compositionally distinct but geochemically linked to the same intrusive system. The host GR define the silica-rich end of the whole-rock array (SiO_2 = 62.7–72.6 wt.%), whereas the MME extend the suite toward lower SiO_2 (49.4–60.5 wt.%) and higher Fe_2O_3, MgO, CaO, and TiO_2. Their rounded to ellipsoidal shapes, finer-grained microgranular textures, locally lobate to crenulate contacts with the host and evidence for shared mineral crystals at enclave margins (e.g., K-feldspar megacryst; Figure 3a1), collectively favor a magmatic origin over incorporation of country-rock xenoliths [50]. Such field, textural and geochemical relations are widely documented in enclave-bearing granitoid systems in which mafic to intermediate magmas interacted with felsic magma reservoirs during pluton assembly [10–13,50]. Clemens [51] emphasized that, on a global scale, true magma mixing between enclave and host magmas is uncommon, as most magmatic enclaves primarily record magma mingling accompanied by variable chemical and/or mechanical hybridization, while the much larger felsic host may remain compositionally little affected. Clemens [51] further

documented the incorporation of host-derived K-feldspar into enclaves as evidence of mechanical hybridization while both magmas remained sufficiently mobile for crystal exchange. In the Kastoria pluton, this occurrence is only limited to the enclave–host contacts, rather than dispersed inside the enclaves, suggesting that this mechanical transfer was relatively restricted.

The MME population is internally heterogeneous. Most enclaves are fine-grained, display sharp contacts with the host GR, and retain disequilibrium microstructures (acicular apatite and amphibole crystals) consistent with thermal quenching upon contact with a cooler, more crystallized host. In contrast, the largest enclave (MET-11E; Figure 3a) is the coarsest-grained and the most silica rich member of the enclave suite (SiO_2 = 60.5 wt.%) and lacks a chilled margin and disequilibrium microstructures. This body is interpreted as the product of an early mafic injection into a still-hot, largely molten granitic reservoir, where the reduced thermal contrast permitted slower crystallization, grain coarsening, and extensive chemical exchange with the host. Particularly diagnostic is the occurrence of K-feldspar megacrysts [52] shared across the contact between MET-11E and the host GR—MET-11 (Figure 3a1). Importantly, the high SiO_2 content of MET-11E should not be interpreted as evidence for advanced fractional differentiation. Although it is the most silica-rich MME (SiO_2 = 60.5 wt.%), it has the lowest K_2O and highest Na_2O contents of the enclave population, indicating decoupling between Si and K enrichment. The microcline megacrysts shared across the MET-11E and MET-11 contact show that K-feldspar was already crystallizing during magma interaction, potentially buffering part of the host K budget in the crystalline assemblage. Prolonged interaction with the felsic host could therefore have increased SiO_2 and Na_2O in MET-11E without corresponding K enrichment. MET-11E is thus better interpreted as a long-residence, extensively hybridized enclave rather than only the most fractionated MME [11,31,50–53].

Taken together, the marked textural differences between MET-11E and the finer-grained MME indicate that the enclave population did not form under a single set of thermal and rheological conditions. The coexistence of a coarse-grained, extensively hybridized enclave with numerous finer-grained, quenched enclaves is consistent with recurrent mafic recharge into a felsic reservoir that evolved progressively during crystallization. In this framework, recharge into a hotter, more melt-rich host would permit more prolonged interaction and slower crystallization, whereas recharge into a cooler and more crystalline host would produce greater thermal contrast and more rapid quenching, producing the fine-grained textures characteristic of most of the MME. The chemical variability of the MME population parallels their textural diversity and defines several broad compositional tendencies rather than discrete groups. These include a SiO_2 and Na_2O rich, strongly hybridized endmember, a relatively Al-rich and less mafic subgroup, a strongly metaluminous subgroup characterized by higher MgO, CaO and compatible-element contents, and a low-SiO_2, Ca–Fe–Ti–P-rich end of the enclave array. Localized enrichments in elements such as Ba and Sr further indicate variable mineral control. Overall, the compositional spread is more consistent with degrees of variable chemical hybridization and crystal accumulation than with evolution along a single mafic injection [11–13,50,51].

This relation suggests that enclave formation was not controlled by a single uniform thermal regime. Rather, the enclave population appears to preserve a range of interaction states, from relatively rapidly chilled mafic injections to more slowly crystallized and more strongly hybridized enclave bodies. This interpretation is further supported by the recent synthesis of enclave-host relationships by Clemens [51], who showed that heterogeneous enclave populations may reflect multiple magma injections and variable degrees of interaction with the host. Comparable variability has been described in other granitoid systems in which repeated mafic replenishment occurred under evolving thermal and rheological conditions within the magmatic reservoir [31,54–57].

5.2. Differentiation and Open-System Evolution of the Pluton

The whole-rock trends demonstrate that magmatic differentiation was an important control on the evolution of the Kastoria pluton. The major-element Harker diagrams define systematic decreases in Fe_2O_3, MgO, TiO_2, CaO, and P_2O_5, with increasing SiO_2 (Figure 8), while compatible elements such as V, Cr, Ni, and Sc likewise decrease from the MME toward the GR (Figure 9). These relations are consistent with progressive removal of ferromagnesian phases, feldspar, Fe-Ti oxides, and apatite during the differentiation [27,58]. Amphibole barometry and Zr-in-titanite thermometry indicate crystallization at pressures of approximately 3 kbar and temperatures of approximately 710 °C, within a shallow- to mid-crustal environment [19]. The similar titanite temperatures recorded in both GR and MME confirm the contemporaneous crystallization and thermal overlap between the interacting magmas during pluton assembly.

Despite these differentiation trends, geochemical data are inconsistent with evolution through closed-system fractional crystallization alone. Al_2O_3, Na_2O, K_2O, and feldspar-compatible elements such as LILE (Rb, Sr, Ba) do not define strict trends but instead show overlap and scatter between GR and MME, particularly within the enclave population (Figure 9). The greater scatter observed in these mobile elements may also partly reflect post-magmatic element redistribution associated with the documented alteration of the pluton [19]. Nevertheless, this behavior contrasts with the much more regular decrease of compatible elements contents and suggests that crystal fractionation operated together with the magma recharge, local crystal accumulation, magma mixing, and incomplete chemical equilibration within an open magmatic system that is evident from the enclaves' appearance [12,50,51,58,59]. The broader geochemical dispersion of the MME relative to the host GR is especially consistent with repeated injections of compositionally distinct, less evolved magma into a crystallizing felsic magma reservoir. Although the GR and MME preserve broadly similar subduction-related signatures, these similarities may reflect inherited characteristics of subduction-modified source components and do not necessarily imply derivation from a single parental melt. The Kastoria pluton is therefore better viewed as an open magmatic system in which felsic differentiation was repeatedly modified by mafic recharge where mingling and hybridization of the enclaves took place [58–60].

The persistence of high-K compositions across the full SiO_2 range of the suite, also expressed mineralogically by the K-feldspar megacrysts in the GR, indicates that the potassic affinity of the system was not produced solely by extreme late-stage felsic differentiation. This is particularly evident in the least evolved MME, which retain relatively high K_2O contents (4.2–4.7 wt.% at SiO_2 < 55 wt.%), suggesting that the mafic to intermediate magma entering the felsic host was already rich in K before enclave hybridization and chemical exchange with the host. This feature is compatible with derivation from, or interaction with, an enriched lithospheric mantle source previously modified by subduction-related metasomatism [26,60,61]. Comparable high-K calc-alkaline enclave-bearing suites have been interpreted as reflecting interaction between felsic crustal melts and potassic mafic inputs from a subduction-enriched mantle source [62,63]. A comparable association is described by Moyen et al. [64], in which MME-bearing calc-alkaline granitoids occur with potassic mafic–intermediate magmas interpreted as melts of modified mantle, supporting the view that the K-rich character of the mafic component may precede its interaction and hybridization with the felsic reservoir.

5.3. REE and Multi-Element Constraints on Magma Evolution

The REE systematics further support the interpretation that the MME and host GR represent related components of the same magmatic system but did not evolve along a single closed-system liquid line of descent. Both lithologies display similar LREE-enriched, HREE-depleted patterns (Figure 10a), but the MME are shifted toward higher REE and retain flatter HREE than the host. The GR, by contrast, show lower total REE abundances and steeper profiles. A broadly comparable mafic–felsic REE contrast is reported from the Variscan KCG (K-feldspar porphyritic Calc-alkaline Granitoids)–vaugnerite association of Moyen et al. [64], where the potassic mafic vaugnerites display consistently high REE abundances and the associated granitoids occupy the lower part of their REE range. The higher REE concentrations of the MME may therefore partly reflect an initially more REE-enriched mafic parental magma, rather than solely differences in the extent of fractional crystallization. Such initial compositional differences could reflect contrasting source contributions to the interacting mafic and felsic magmas, subsequently modified by mineral fractionation and variable degrees of magma interaction [60,64]. A notable feature is the progressive decrease in ΣREE with increasing SiO_2, which is preserved within the GR population itself. Although REE commonly behave incompatibly during early silicate fractionation, their concentration may decrease once minerals with high REE partition coefficients are early crystallizing mineral phases [30,45,58].

The widespread occurrence of magmatic apatite, titanite, allanite, and zircon throughout the Kastoria pluton suggests that accessory-phase saturation began relatively early in the crystallization sequence rather than being restricted to the most evolved felsic melts. In particular, euhedral accessory crystals occurring in direct contact with early magmatic phases, together with zircon inclusions enclosed within amphibole, indicate that at least part of the accessory assemblage was already crystallizing during relatively early stages of magma evolution [19]. Their subsequent crystallization and segregation provide a plausible mechanism for the progressive decrease in ΣREE, Y, Zr, Hf, and P_2O_5 toward more silicic compositions [19,45,46]. Amphibole preferentially incorporates MREE more strongly than HREE, so its fractionation may decrease MREE/HREE ratios in residual melts [30]. The REE evolution of the suite therefore appears to have been increasingly controlled by amphibole and the accessory assemblage, rather than following the simple incompatible-element enrichment expected during fractionation of the major silicate phases alone [45,46,65]; comparable accessory-phase control on REE budgets in felsic magmas was demonstrated by Moyen et al. [64]. MET-04 represents the evolved extreme end of this trend. Its very low ΣREE, La, Th, Y, Zr, Hf, and P_2O_5 contents are consistent with strong prior control by allanite, titanite, apatite, and zircon during differentiation. This also explains its position in Figure 14c, where the very low La content drives MET-04 toward exceptionally high Ba/La values rather than indicating unusually strong Ba enrichment.

The Eu negative anomaly is weak to none in both lithologies. Mean Eu/Eu* is approximately 0.90 for the GR (range 0.73–1.12) and 0.86 for the MME (range 0.65–1.12). Such subtle Eu anomalies may suggest that plagioclase did not exert a dominant control on the earlier stages of magma evolution, because progressive removal of plagioclase, which preferentially incorporates Eu and Sr, would normally generate increasingly negative Eu anomalies and stronger Sr depletion in residual melts. Weak Eu anomalies, relatively high Sr contents and moderately elevated Sr/Y ratios are instead compatible with an earlier, relatively deep stage of melt generation or differentiation under plagioclase-poor conditions, potentially involving garnet ± amphibole in the residue. Subsequent plagioclase crystallization clearly affected the evolving magmas, as suggested by the weak decrease and considerable scatter of Sr with increasing SiO_2 and by slightly positive Eu anomalies in some less evolved GR.

The primitive mantle-normalized multi-element patterns (Figure 10b) preserve both an inherited source signature and a superimposed differentiation point. Both GR and MME display LILE enrichment and Nb–Ta–Ti depletion, consistent with inheritance from a subduction-modified magmatic source [66,67]. Superimposed on this common pattern, however, the GR show progressively stronger depletion in P and Ti and lower Y, Zr, Hf, and REE abundances relative to the MME. These behaviors parallel the systematic decreases in P_2O_5, TiO_2, Y, Zr, Hf, and ΣREE with increasing SiO_2, and they record increasing mineral control during felsic differentiation, involving apatite, Fe–Ti oxides, and titanite, together with zircon and allanite. The multi-element patterns thus preserve a subduction-related source inheritance while simultaneously recording its progressive modification by amphibole- and accessory-phase-controlled differentiation within the crustal magma reservoir [33,45,46,58].

5.4. Peraluminosity and the I-Type Affinity of the Kastoria Pluton

Peraluminosity, defined by A/CNK > 1.0, has traditionally been used as an indicator of S-type (sediment-derived) granitoids, although alumina saturation should not by itself be a genetic criterion. Chappell et al. [68] emphasized that the metaluminous–peraluminous boundary is descriptive rather than petrogenetic and documented that peraluminous compositions are common among I-type granitoids. In the Lachlan Fold Belt, nearly half of the analyzed I-type granites are peraluminous, and numerous individual suites extend continuously from metaluminous mafic to peraluminous felsic compositions. Peraluminous I-type granitoids therefore do not require sedimentary protoliths, and experimental work along with natural observations demonstrate that peraluminous felsic melts can be generated from partial melting of igneous rocks through incongruent breakdown of hydrous minerals, particularly amphibole and biotite [68,69]. Wang et al. [70] documented strongly peraluminous compositions (A/CNK = 1.19–1.32) in highly fractionated I-type granites, further demonstrating that alumina saturation must be evaluated together with mineralogical and whole-rock geochemical characteristics rather than used independently for genetic classification.

The Kastoria rocks show a comparable overlap in alumina saturation. The GR range from metaluminous to moderately peraluminous compositions (A/CNK = 0.92–1.44; average of 1.12), with 43 of 51 samples having A/CNK > 1.0, whereas the MME are metaluminous, with only one enclave extending slightly into the peraluminous field (Figure 7). A relevant Variscan comparison is provided by Moyen et al. [64], whose KCG similarly extend from metaluminous to moderately peraluminous compositions (approximately A/CNK = 0.9–1.4; see Figure 2c in [64]), despite their genetic association with potassic mafic magmatism. Their enclave population spans past the metaluminous–peraluminous boundary, showing that peraluminous signatures are not restricted to granitoid hosts. Importantly, Moyen et al. [64] demonstrated that granitoids from contrasting sources may converge toward mildly peraluminous compositions near the granitic minimum and cautioned against using a fixed A/CNK threshold as a source discriminator.

Importantly, this increase in A/CNK is accompanied in the Kastoria pluton by a pronounced decrease in P_2O_5 with increasing SiO_2. The combination of a positive A/CNK–SiO_2 relationship and a negative P_2O_5–SiO_2 relationship has been identified as characteristic of I-type granite evolution, in contrast to the different phosphorus behavior commonly observed in S-type granitic melts [70–72]. These trends are not uniquely diagnostic, however, because some evidently S-type granites may develop comparable relationships during differentiation as documented by Gao et al. [72]. The inferred I-type affinity of the Kastoria pluton therefore lies on the combined mineralogical and geochemical evidence rather than on alumina saturation alone. Hornblende-bearing assemblages, the association of the GR with predominantly metaluminous MME, the high-K calc-alkaline affinity,

and the absence of characteristic strongly peraluminous minerals such as primary muscovite, cordierite and garnet collectively favor an I-type affinity [64,68,70,72].

5.5. Tectonomagmatic Setting

The tectonomagmatic discrimination diagrams consistently place the Kastoria pluton within an orogenic compositional range extending from volcanic-arc to collisional and late-orogenic affinities. In the trace-element diagrams of Pearce et al. [33] (Figure 11a–d), the GR plot predominantly within the volcanic-arc granite field or close to the volcanic-arc–syn-collisional boundary, whereas the MME broadly overlap the GR but extend toward higher Y, Nb, Yb and Ta concentrations without defining a distinct within-plate population. Similarly, the Th/Ta–Yb relations place most samples within the active continental-margin field [36] (Figure 11e). The Rb/30–Hf–Ta*3 diagram (Figure 12a) extends this distribution from volcanic-arc toward syn-collisional and late/post-collisional compositions, whereas the R1–R2 systematics (Figure 12b) place the GR mainly within the syn-collisional to late-orogenic fields and the MME toward the post-collision uplift field [33,36–38].

These partly overlapping classifications should not be interpreted as recording a literal temporal progression from volcanic arc to collisional magmatism. The discrimination fields are empirical and should therefore be interpreted with caution, as whole-rock compositions may reflect inherited source signatures and subsequent magmatic differentiation. This ambiguity is particularly relevant to late-orogenic granitoids. Moyen et al. [64] showed that trace-element and REE characteristics of oceanic-arc and late-collisional Variscan granitoids may overlap substantially and cautioned that their KCG could consequently be misinterpreted as late-subduction magmas if the complete magmatic association were ignored. Instead, these KCG are interpreted as derivatives of potassic mafic magmas generated from previously modified mantle in a late-collisional system [64]. Thus, calc-alkaline granitoids emplaced during late- to post-collisional stages may preserve geochemical characteristics inherited from earlier subduction-related source modification, making discrimination between active-arc and later collisional magmatism from whole-rock geochemistry alone uncertain. This is supported by Schenker et al. [6] as well. Accordingly, the classical diagrams are most appropriately interpreted as indicating a broader convergent-to-collisional orogenic affinity, with the Kastoria pluton extending toward late/post-collisional characteristics, rather than independently identifying a specific geodynamic mechanism [33,37,38,64].

The Whalen and Hildebrand [34] discrimination diagrams (Figure 13a) provide a more process-oriented comparison, with the dataset plotting toward the "slab-failure" field. Nevertheless, this result requires cautious interpretation, because their principal discrimination criteria were calibrated using granitoids with 55–70 wt.% SiO_2 and ASI < 1.1; portions of this study's data fall outside that compositional window. More importantly, geochemical discrimination diagrams cannot independently resolve the geometry or precise mechanism of slab disruption. The association with the slab-failure field should therefore not be regarded as direct evidence for complete slab break-off. Rather, the result is significant in showing that the Kastoria pluton resembles granitoid suites generated after the transition away from steady-state arc magmatism and during post-collisional lithospheric reorganization. In this sense, the slab-failure affinity is compatible with disturbance of the previously established subduction system, potentially involving localized slab tearing, progressive or partial detachment, without requiring complete slab break-off.

Taken together, the tectonomagmatic constraints indicate that the ca. 300 Ma Kastoria pluton preserves a clear volcanic-arc inheritance, consistent with earlier subduction of oceanic lithosphere beneath a continental margin, while its overall geochemical and

regional context is more consistent with collisional to late/post-collisional magmatism [33,34,36–38].

5.6. Source Characteristics, High Sr/Y Affinity, and Subduction-Related Signature

Elevated Sr/Y and La/Yb ratios, accompanied by low Y and HREE contents, have long been used as characteristic geochemical criteria for recognizing adakitic magmas and distinguishing them from normal arc andesite–dacite–rhyolite suites [43,73]. In the original model, these features were attributed to melting of subducted oceanic crust under conditions in which garnet remained stable and plagioclase was absent from the residue, thereby retaining Y and HREE while allowing Sr to preferentially enter the melt. Subsequent classifications broadened these criteria and contributed to widespread identification of "adakitic" rocks on the basis of whole-rock trace-element systematics [40,43,74].

However, the genetic significance of those criteria has been increasingly questioned. Moyen [42] emphasized that high Sr/Y and La/Yb ratios are not uniquely diagnostic of adakite genesis and may be produced by several distinct processes, including melting of compositionally favorable sources, deep melting with residual garnet, fractional crystallization or assimilation–fractional crystallization, and interaction between felsic melts and mantle material. Moyen [75] reiterated this point even more explicitly, arguing that the term adakite had been applied to an excessively broad range of rocks whose only common feature was commonly high—or even moderate—Sr/Y and La/Yb ratios, and that classification based on these criteria alone is misleading because major-element composition and the broader petrogenetic context must also be considered. Thus, an "adakitic signature" neither demonstrates slab melting nor uniquely constrains the depth or tectonic setting of magma generation. Castillo [44] similarly stressed the diversity of processes capable of producing adakite-like trace-element characteristics, making genetic interpretations based solely on discrimination fields problematic.

The Kastoria pluton suggests this ambiguity particularly well. Part of the GR satisfies commonly applied high Sr/Y criteria and plots on or overlaps compositional fields conventionally associated with adakites and high-Al TTD (Figure 14a). The MME plot predominantly within the normal arc ADR field (Figure 14a). The average GR is displaced toward lower Y and higher Sr/Y relative to the average MME. The $(La/Yb)_{CN}$ versus Yb_{CN} diagram (Figure 14b), however, does not reproduce the same degree of separation. The GR generally have higher $(La/Yb)_{CN}$ than the MME, consistent with the steeper REE patterns observed in Figure 10a, but both lithological groups plot predominantly in the normal arc ADR field rather than defining a coherent population within the adakite–high-Al TTD field. The Sr/Y and REE criteria are therefore only partly coupled. Subsequently, the overlap with an adakite field should not be dismissed as geochemically meaningless, but neither should it be used as sufficient grounds for classifying the rocks as adakitic. This study's interpretation is that Kastoria pluton exhibits a moderate high Sr/Y affinity, the petrogenetic significance of which must be assessed independently of the adakite label [40,42,44].

The high Sr/Y tendency remains petrogenetically informative when considered together with the relatively low Y and HREE abundances and weak to no Eu negative anomalies. These features are compatible with a relatively deep and plagioclase-poor magma source with differentiation and possible retention of garnet ± amphibole, in which Y and HREE were preferentially retained in the residue with Sr going in the melt. Subsequent shallower differentiation involving amphibole and REE-bearing accessory phases could further modify the Y–REE signature. The ca. 3 kbar amphibole crystallization pressure [19] record a later crustal stage and do not preclude earlier evolution at greater depth that may reflect a polybaric history rather than a single high-pressure process [40,42,44,76].

The Ba/La-Th/Yb systematics (Figure 14c) provide complementary information on the nature of the magma source. Such source-sensitive ratios are most appropriately evaluated in the least evolved compositions, where the effects of fractional crystallization are minimized [41]. The MME therefore provide the closest available approximation to the mafic input to the system, although they cannot be regarded as unmodified primary mantle melts because enclave hybridization with their host has been described before (see Section 5.1) [12,50]. Except for the Ba-rich TH-16E sample, the MME show relatively high Th/Yb at modest Ba/La and plot predominantly along the "sediment or sediment-melt" direction defined from [41] (Figure 14c). A comparable tendency is obtained in the Ba/Th–$(La/Sm)_{CN}$ framework of Elliott [49]. Thus, in the conventional interpretation, the least evolved Kastoria compositions favor a stronger sediment melt-related than fluid-dominated contribution to the mantle source [41,49].

Plank [77] showed that Th/La varies substantially among subducting sediments and can be transferred into arc magmas with remarkably little fractionation, allowing arc magmas to inherit sedimentary Th–REE characteristics. REE and Th may furthermore reflect relatively high-temperature, melt-like transfer from the subducting plate, and in some arcs even part of the characteristic low-Nb/high-Th signature may be inherited directly from recycled sediment. The relatively high Th/Yb of the Kastoria MME is therefore consistent with a subduction-modified lithospheric mantle source, potentially involving sediment-derived melt or another high-temperature melt-like transfer agent [41,49,77].

The precise physical form of this sedimentary contribution nevertheless remains uncertain. Th/Yb–Ba/La does not uniquely distinguish direct sediment melting from other modes of sediment recycling, and the ratios may subsequently be modified by differentiation and magma interaction, as demonstrated by the evolved GR and the contrasting high-Ba/La samples discussed in Section 4.5. Turner and Langmuir [78] further questioned the uniqueness of the traditional sediment-melt versus altered-oceanic-crust-fluid model, emphasizing the effects of variable sediment composition and mantle-wedge heterogeneity. Accordingly, the studied data provide stronger evidence for a sediment-influenced, subduction-modified source than for a uniquely identifiable sediment-melt transfer mechanism [77,78].

A useful Variscan analogue is provided by appinite–vaugnerite–granitoid associations in the NW Iberian Massif. Galán et al. [79] interpreted their mafic magmas as products of partial melting of heterogeneous lithospheric mantle previously metasomatized in a supra-subduction environment and explicitly considered sediment and/or sediment-derived melts as contributors to this metasomatism. Importantly, they further proposed that, after slab break-off, asthenospheric upwelling beneath the previously metasomatized lithosphere could trigger partial melting of both lithospheric mantle and lower crust. This model demonstrates that a strong inherited subduction and sedimentary signature can be preserved in mafic–felsic magmatism generated later under syn- to post-collisional conditions.

Collectively, the moderate high-Sr/Y affinity, evidence for relatively deep and plagioclase-poor early magma evolution, sediment melt-related signature, and broader arc-like trace-element inheritance are consistent with melting of an enriched lithospheric source previously modified during subduction. This provides a petrogenetic connection with the late/post-collisional and slab-failure affinities identified in Section 5.5. Disruption of the established subduction system could have promoted asthenospheric upwelling and thermal disturbance of previously metasomatized lithospheric mantle and lower crust, triggering renewed melting while preserving their inherited arc-related geochemical characteristics. Localized slab tearing, progressive or partial detachment, or a related slab failure therefore represents a plausible framework for the Kastoria magmatism [34,60,79].

5.7. Regional Context and Diachronous Late Variscan Tectonomagmatic Reorganization

The regional significance of the Kastoria pluton becomes clearer when its ca. 300 Ma emplacement is considered within the diachronous evolution of the Variscan orogen [3,80]. Variscan magmatism in the Balkan sector of central Bulgaria spans ca. 315–285 Ma, distinctly younger than much of the ca. 340–320 Ma post collisional magmatism of Central Europe and broadly comparable in age to the younger granitoid record of Iberia [80]. Carrigan et al. [80] suggested that collision and associated magmatism culminated earlier in the central and northern Variscides and progressed toward the eastern, western, and southern sectors of the orogen. This diachroneity is consistent with the broader complexity of Variscan convergence and subduction-zone reorganization emphasized by Kroner and Romer [3] and indicates that broadly coeval granitoids need not record the same suture, slab system or tectonic stage.

The Pelagonian basement forms part of this younger southeastern Variscan record. Schenker et al. [6] documented widespread late- to post-Variscan calc-alkaline granitoids at ca. 315–301 Ma, followed by subvolcanic magmatism at ca. 280 Ma and increasing mantle-derived input during Early Permian extension. Kastoria pluton therefore lies near the young end of the main Late Carboniferous event, preceding the clearer Early Permian shift toward mantle-influenced extensional magmatism. Further south, granitoids of central Pelagonian zone yield predominantly ca. 290–280 Ma ages, with magmatism continuing to ca. 270 Ma, demonstrating a magmatic history lasting at least ca. 30 Ma [5]. Particularly relevant is the nearby ca. 300 ± 3 Ma Voras plutonic complex, which also contains MME and was directly compared with the Kastoria and Varnountas plutons by Koroneos et al. [81]. Kastoria pluton forms part of a broader and prolonged Late Carboniferous–Early Permian magmatic event in the Pelagonian zone [5,6,81].

The tectonic significance of this magmatism remains debated. Vavassis et al. [82] interpreted Late Carboniferous calc-alkaline magmatism in Evia as related to northward Palaeotethyan subduction beneath the Eurasian margin, followed by ridge subduction, slab detachment and Permian extension. In contrast, Schenker et al. [6] emphasized the absence of Late Carboniferous accretionary complexes, blueschists, or eclogites, as well as deep forearc basins in the Balkans, and cautioned that post-collisional magmatism may retain geochemical characteristics indistinguishable from those of active volcanic arcs. The wider Balkan record likewise demonstrates substantial spatial variability: a ca. 326 Ma syn-collisional granitoid in the East Serbian Carpatho-Balkanides was followed by post-collisional plutonism between ca. 323 and 290 Ma [83], whereas broadly contemporaneous granitoids in central Bulgaria were attributed to continued subduction after terrane juxtaposition [80], and ca. 302 Ma magmatism in the Eastern Pontides developed during extension within an active Palaeotethyan subduction system [62]. Spahić et al. [9] distinguished the Inner Carpathian–Balkan Rheic suture, where collision was followed by slab breakoff and post-collisional exhumation, from an external Variscan Palaeotethyan suture extending through the Balkan–Hellenides sector. In their reconstruction, the Palaeotethys remained only partly closed during the Late Carboniferous and continued toward the Hellenides, cautioning against directly transferring the Rheic slab-breakoff history to the Pelagonian zone. Thus, although their Rheic slab-breakoff model cannot be transferred directly to Pelagonia, it demonstrates that localized slab failure could accompany Late Variscan tectonomagmatic reorganization without requiring synchronous terminal closure of the entire Palaeotethyan ocean.

Within this regional framework, the geochemical characteristics of the Kastoria pluton are consistent with magmatism during reorganization of a previously established subduction system. The subduction-modified source signature, high Sr/Y affinity compatible with an earlier relatively deep and hydrous stage of magma evolution characterized by limited plagioclase and amphibole ± garnet control, recurrent mafic recharge recorded by

the MME, and late/post-collisional tectonomagmatic affinity collectively favor renewed involvement of previously modified lithospheric reservoirs rather than simple steady-state arc magmatism. Slab disruption could provide a mechanism for such reactivation: progressive removal or failure of the subducting lithosphere permits asthenospheric upwelling and thermal perturbation of metasomatized lithospheric mantle and lower crust, generating renewed mantle and crustal melting while retaining inherited subduction-related geochemical characteristics [6,84]. The predominant slab-failure affinity of both GR and MME (Figures 11a,c and 13a) is consistent with this interpretation but does not uniquely resolve the geometry of slab disruption. Localized tearing, progressive or partial detachment, and complete slab breakoff therefore remain possible expressions of the same broader process, while the whole-rock data primarily constrain the magmatic response to lithospheric reorganization rather than the geometry of the failing slab [34,84].

Comparable associations elsewhere in the Variscan belt reinforce this process-level interpretation. In the eastern French Massif Central, late-collisional potassic calc-alkaline granitoids occur with mantle-derived Mg–K vaugneritic magmas. Moyen et al. [64] interpreted the wider late-orogenic association as reflecting concurrent crustal and mantle melting, with the mafic magmas derived from mantle previously enriched by crustal material, potentially during preceding subduction, and linked its development to slab retreat and lithospheric thinning. In northwestern Iberia. Galán et al. [79] similarly interpreted appinites and vaugnerites as products of partial melting of subduction-metasomatized lithospheric mantle and considered asthenospheric upwelling following slab breakoff as a possible trigger for melting of both the enriched mantle and lower crust. MMEs in other post-collisional batholiths likewise provide evidence for substantial mantle involvement in granitoid generation (Gómez-Frutos and Castro [85]). The Corsica–Sardinia Batholith provides a complementary example in which slab detachment, lithospheric delamination, shear heating, and advection of mantle-derived melts have been evaluated as mechanisms capable of raising the late-Variscan geotherm and promoting crustal and upper-mantle melting (Casini et al. [86]). These systems are not direct tectonic equivalents of Kastoria, but collectively show that mantle-derived mafic input, reworking of previously modified lithospheric reservoirs, and crust–mantle interaction were recurrent features of late Variscan tectonomagmatic reorganization.

6. Conclusions

(1) The ca. 300 Ma Kastoria pluton represents a composite high-K calc-alkaline with characteristics consistent with an I-type affinity assembled through open-system interaction between felsic and mafic–intermediate magma. The offset GR–MME compositions, enclave textures, and variable degrees of chemical exchange record recurrent mafic recharge, magma mingling, limited hybridization, and differentiation.

(2) Magmatic differentiation involved progressively stronger control by amphibole and accessory minerals. Decreasing ΣREE, Y, Zr, Hf, and P_2O_5 toward the evolved GR, together with petrographic evidence for early crystallization of apatite, titanite, allanite and zircon, indicate that accessory-phase fractionation substantially modified the REE–HFSE budget of the felsic magmas.

(3) The GR display a moderate high-Sr/Y affinity but do not constitute a classical adakite suite. Their partly decoupled Sr/Y and REE systematics, relatively low Y–HREE contents, and weak to absent negative Eu anomalies are compatible with an earlier potentially deeper stage of magma evolution involving limited plagioclase control and possible garnet ± amphibole involvement, followed by shallower differentiation. The least evolved MME additionally preserve a high-K, subduction-modified source signature. The precise sediment melt-transfer mechanism cannot be uniquely resolved with the present data and would benefit from additional Sr–Nd isotopic constraints.

(4) Kastoria pluton records late/post-collisional Variscan magmatism that retained geochemical characteristics inherited from an earlier convergent-margin system. Its arc-like trace-element inheritance, recurrent mafic input and predominant slab-failure affinity are consistent with renewed mantle–crust magmatism during disruption of an established subduction system and lithospheric reorganization. Slab breakoff provides a plausible mechanism for this thermal reorganization, although complete detachment cannot be uniquely distinguished from localized tearing or progressive slab failure. The Kastoria pluton therefore provides an example of how subduction-modified lithospheric sources can be reactivated during the diachronous late Variscan reorganization in Greece.

Supplementary Materials: The following supporting information can be downloaded at: https://www.mdpi.com/article/10.3390/min16111125/s1, File S1: Whole rock WD-XRF and LA-ICP-MS analytical data.

Author Contributions: Data curation, I.G.; writing—original draft, I.G.; writing—review and editing, A.K., L.P., A.C., K.P. and V.G. All authors have read and agreed to the published version of the manuscript.

Funding: This research received no external funding.

Data Availability Statement: Data are contained within the article and Supplementary Materials.

Conflicts of Interest: The authors declare no conflicts of interest.

References

1. Finger, F.; Roberts, M.P.; Haunschmid, B.; Schermaier, A.; Steyrer, H.P. Variscan Granitoids of Central Europe: Their Typology, Potential Sources and Tectonothermal Relations. *Mineral. Petrol.* **1997**, *61*, 67–96. https://doi.org/10.1007/BF01172478.
2. Nance, R.D.; Gutiérrez-Alonso, G.; Keppie, J.D.; Linnemann, U.; Murphy, J.B.; Quesada, C.; Strachan, R.A.; Woodcock, N.H. Evolution of the Rheic Ocean. *Gondwana Res.* **2010**, *17*, 194–222. https://doi.org/10.1016/j.gr.2009.08.001.
3. Kroner, U.; Romer, R.L. Two Plates—Many Subduction Zones: The Variscan Orogeny Reconsidered. *Gondwana Res.* **2013**, *24*, 298–329. https://doi.org/10.1016/j.gr.2013.03.001.
4. Barbarin, B. A Review of the Relationships between Granitoid Types, Their Origins and Their Geodynamic Environments. *Lithos* **1999**, *46*, 605–626. https://doi.org/10.1016/S0024-4937(98)00085-1.
5. Reischmann, T.; Kostopoulos, D.K.; Loos, S.; Anders, B.; Avgerinas, A.; Sklavounos, S.A. Late Palaeozoic Magmatism in the Basement Rocks Southwest of Mt. Olympos, Central Pelagonian Zone, Greece: Remnants of a Permo-Carboniferous Magmatic Arc. *Geosociety* **2001**, *34*, 985. https://doi.org/10.12681/bgsg.17134.
6. Schenker, F.L.; Burg, J.-P.; Kostopoulos, D.; Moulas, E.; Larionov, A.; von Quadt, A. From Mesoproterozoic Magmatism to Collisional Cretaceous Anatexis: Tectonomagmatic History of the Pelagonian Zone, Greece. *Tectonics* **2014**, *33*, 1552–1576. https://doi.org/10.1002/2014TC003563.
7. Mountrakis, D.M. Structural Geology of the North Pelagonian Zone s.l. and Geotectonic Evolution of the Internal Hellenides (Macedonia, Greece). Ph.D. Thesis, Aristotle University of Thessaloniki, Thessaloniki, Greece, 1983.
8. Zlatkin, O.; Avigad, D.; Gerdes, A. The Pelagonian Terrane of Greece in the Peri-Gondwanan Mosaic of the Eastern Mediterranean: Implications for the Geological Evolution of Avalonia. *Precambrian Res.* **2017**, *290*, 163–183. https://doi.org/10.1016/j.precamres.2017.01.005. 1.
9. Spahić, D.; Tančić, P.; Kurešević, L.; Milovanović, D. Variscan Sutures in the Carpathian-Balkan Belt Revisited: A Granitoid Perspective on Late Palaeozoic Closure of the Rheic Ocean, Slab Breakoff and Tectonic Exhumation. *Int. Geol. Rev.* **2026**, *68*, 769–807. https://doi.org/10.1080/00206814.2025.2607024.
10. Vernon, R.H. Microgranitoid Enclaves in Granites—Globules of Hybrid Magma Quenched in a Plutonic Environment. *Nature* **1984**, *309*, 438–439. https://doi.org/10.1038/309438a0.
11. Barbarin, B.; Didier, J. Genesis and Evolution of Mafic Microgranular Enclaves through Various Types of Interaction between Coexisting Felsic and Mafic Magmas. *Earth Environ. Sci. Trans. R. Soc. Edinb.* **1992**, *83*, 145–153. https://doi.org/10.1017/S0263593300007835.

12. Perugini, D.; Poli, G. The Mixing of Magmas in Plutonic and Volcanic Environments: Analogies and Differences. *Lithos* **2012**, *153*, 261–277. https://doi.org/10.1016/j.lithos.2012.02.002.
13. Clemens, J.D.; Elburg, M.A.; Harris, C. Origins of Igneous Microgranular Enclaves in Granites: The Example of Central Victoria, Australia. *Contrib Miner. Pet.* **2017**, *172*, 88. https://doi.org/10.1007/s00410-017-1409-2.
14. Mountrakis, D. Structural Evolution of the Pelagonian Zone in Northwestern Macedonia, Greece. *SP* **1984**, *17*, 581–590. https://doi.org/10.1144/GSL.SP.1984.017.01.45.
15. Mountrakis, D. The Pelagonian Zone in Greece: A Polyphase-Deformed Fragment of the Cimmerian Continent and Its Role in the Geotectonic Evolution of the Eastern Mediterranean. *J. Geol.* **1986**, *94*, 335–347. https://doi.org/10.1086/629033.
16. Papanikolaou, D. Timing of Tectonic Emplacement of the Ophiolites and Terrane Paleogeography in the Hellenides. *Lithos* **2009**, *108*, 262–280. https://doi.org/10.1016/j.lithos.2008.08.003.
17. Pe-Piper, G.; Piper, D.J.W. *The Igneous Rocks of Greece: The Anatomy of an Orogen; Beiträge zur Regionalen Geologie der Erde*; Gebüder Borntraeger: Berlin Stuttgart, 2002; ISBN 978-3-443-11030-7.
18. Grigoriadou, A.; Koroneos, A.; Eleftheriadis, G. Mineralogy of The Kastoria pluton (W. Macedonia). *Bull. Geol. Soc. Greece* **2003**, *35*, 46–60.
19. Gerontidou, I.; Koroneos, A.; Papadopoulou, L.; Chatzipetros, A.; Masotta, M.; Karampelas, S. Magmatic to Subsolidus Evolution of the Variscan Kastoria Pluton (NW Greece): Constraints from Mineral Chemistry and Textures. *Minerals* **2026**, *16*, 83. https://doi.org/10.3390/min16010083.
20. Kilias, A. The Alpine Geological History of the Hellenides from the Triassic to the Present—Compression vs. Extension, a Dynamic Pair for Orogen Structural Configuration: A Synthesis. *Geosciences* **2024**, *14*, 10. https://doi.org/10.3390/geosciences14010010.
21. Gerontidou, I.; Koroneos, A. Major and trace element analysis on geological samples using WDXRF on pressed pellets. In Proceedings of the 17th GSG International Congress, Myteline, Greece, 28–31 May 2025.
22. Guillong, M.; Meier, D.; Murray, A.; Heinrich, C.; Yardley, B. SILLS: A MATLAB-based program for the reduction of laser ablation ICP-MS data of homogeneous materials and inclusions. *Mineral. Assoc. Can.* **2008**, *40*, 328–333.
23. Streckeisen, A. Classification and Nomenclature of Plutonic Rocks Recommendations of the IUGS Subcommission on the Systematics of Igneous Rocks. *Geol Rundsch* **1974**, *63*, 773–786. https://doi.org/10.1007/BF01820841.
24. Whalen, J.B.; Frost, C.D. The Q-ANOR Diagram: A Tool for the Petrogenetic and Tectonomagmatic Characterization of Granitic Suites. *Geol. Soc. Am.* **2013**, *45*, 24.
25. Irvine, T.N.; Baragar, W.R.A. A Guide to the Chemical Classification of the Common Volcanic Rocks. *Can. J. Earth Sci.* **1971**, *8*, 523–548. https://doi.org/10.1139/e71-055.
26. Peccerillo, A.; Taylor, S.R. Geochemistry of Eocene Calc-Alkaline Volcanic Rocks from the Kastamonu Area, Northern Turkey. *Contr. Mineral. Petrol.* **1976**, *58*, 63–81. https://doi.org/10.1007/BF00384745.
27. Frost, B.R.; Barnes, C.G.; Collins, W.J.; Arculus, R.J.; Ellis, D.J.; Frost, C.D. A Geochemical Classification for Granitic Rocks. *J. Petrol.* **2001**, *42*, 2033–2048. https://doi.org/10.1093/petrology/42.11.2033.
28. Maniar, P.D.; Piccoli, P.M. Tectonic Discrimination of Granitoids. *Geol. Soc. Am. Bull.* **1989**, *101*, 635–643. https://doi.org/10.1130/0016-7606(1989)101%3C0635:TDOG%3E2.3.CO;2.
29. Shand, S.J. *Eruptive Rocks: Their Genesis, Composition, Classification, and Their Relation to Ore Deposits with a Chapter on Meteorites*, 3rd ed.; John Wiley and Sons: New York, NY, USA, 1947.
30. Rollinson, H.; Pease, V. *Using Geochemical Data: To Understand Geological Processes*, 2nd ed.; Cambridge University Press: Cambridge, UK, 2021; ISBN 978-1-108-77783-4.
31. Slaby, E.; Martin, H. Mafic and Felsic Magma Interaction in Granites: The Hercynian Karkonosze Pluton (Sudetes, Bohemian Massif). *J. Petrol.* **2007**, *49*, 353–391. https://doi.org/10.1093/petrology/egm085.
32. Sun, S.-s.; McDonough, W.F. Chemical and Isotopic Systematics of Oceanic Basalts: Implications for Mantle Composition and Processes. *SP* **1989**, *42*, 313–345. https://doi.org/10.1144/GSL.SP.1989.042.01.19.
33. Pearce, J.A.; Harris, N.B.W.; Tindle, A.G. Trace Element Discrimination Diagrams for the Tectonic Interpretation of Granitic Rocks. *J. Petrol.* **1984**, *25*, 956–983. https://doi.org/10.1093/petrology/25.4.956.
34. Whalen, J.B.; Hildebrand, R.S. Trace Element Discrimination of Arc, Slab Failure, and A-Type Granitic Rocks. *Lithos* **2019**, *348–349*, 105179. https://doi.org/10.1016/j.lithos.2019.105179.
35. Chen, W.-F.; Zhang, Q.; Yang, J.; Wang, E.-T.; Song, G.-R.; Jiao, S.-T.; Yuan, J. Trace Element Tectonic Discrimination of Granitoids: Inspiration from Big Data Analytics. *Big Earth Data* **2023**, *7*, 1094–1119. https://doi.org/10.1080/20964471.2023.2222940.

36. Gorton, M.P.; Schandl, E.S. From Continents to Island Arcs: A Geochemical Index of Tectonic Setting for Arc-Related and Within-Plate Felsic to Intermediate Volcanic Rocks. *Can. Mineral.* **2000**, *38*, 1065–1073. https://doi.org/10.2113/gscanmin.38.5.1065.
37. Harris, N.B.W.; Pearce, J.A.; Tindle, A.G. Geochemical Characteristics of Collision-Zone Magmatism. *SP* **1986**, *19*, 67–81. https://doi.org/10.1144/GSL.SP.1986.019.01.04.
38. Batchelor, R.A.; Bowden, P. Petrogenetic Interpretation of Granitoid Rock Series Using Multicationic Parameters. *Chem. Geol.* **1985**, *48*, 43–55. https://doi.org/10.1016/0009-2541(85)90034-8.
39. Defant, M.J.; Richerson, P.M.; De Boer, J.Z.; Stewart, R.H.; Maury, R.C.; Bellon, H.; Drummond, M.S.; Feigenson, M.D.; Jackson, T.E. Dacite Genesis via Both Slab Melting and Differentiation: Petrogenesis of La Yeguada Volcanic Complex, Panama. *J. Petrol.* **1991**, *32*, 1101–1142. https://doi.org/10.1093/petrology/32.6.1101.
40. Martin, H. Adakitic Magmas: Modern Analogues of Archaean Granitoids. *Lithos* **1999**, *46*, 411–429. https://doi.org/10.1016/S0024-4937(98)00076-0.
41. Woodhead, J.D.; Hergt, J.M.; Davidson, J.P.; Eggins, S.M. Hafnium Isotope Evidence for 'Conservative' Element Mobility during Subduction Zone Processes. *Earth Planet. Sci. Lett.* **2001**, *192*, 331–346. https://doi.org/10.1016/S0012-821X(01)00453-8.
42. Moyen, J.-F. High Sr/Y and La/Yb Ratios: The Meaning of the "Adakitic Signature." *Lithos* **2009**, *112*, 556–574. https://doi.org/10.1016/j.lithos.2009.04.001.
43. Drummond, M.S.; Defant, M.J. A Model for Trondhjemite-Tonalite-Dacite Genesis and Crustal Growth via Slab Melting: Archean to Modern Comparisons. *J. Geophys. Res.* **1990**, *95*, 21503–21521. https://doi.org/10.1029/JB095iB13p21503.
44. Castillo, P.R. Adakite Petrogenesis. *Lithos* **2012**, *134–135*, 304–316. https://doi.org/10.1016/j.lithos.2011.09.013.
45. Bea, F. Residence of REE, Y, Th and U in Granites and Crustal Protoliths; Implications for the Chemistry of Crustal Melts. *J Petrol.* **1996**, *37*, 521–552. https://doi.org/10.1093/petrology/37.3.521.
46. Piccoli, P.; Candela, P.; Rivers, M. Interpreting Magmatic Processes from Accessory Phases: Titanite—A Small-Scale Recorder of Large-Scale Processes. *Earth Environ. Sci. Trans. R. Soc. Edinb.* **2000**, *91*, 257–267. https://doi.org/10.1017/S0263593300007422.
47. Peytcheva, I.; Von Quadt, A.; Georgiev, N.; Ivanov, Z.; Heinrich, C.A.; Frank, M. Combining Trace-Element Compositions, U–Pb Geochronology and Hf Isotopes in Zircons to Unravel Complex Calcalkaline Magma Chambers in the Upper Cretaceous Srednogorie Zone (Bulgaria). *Lithos* **2008**, *104*, 405–427. https://doi.org/10.1016/j.lithos.2008.01.004.
48. Wen, D.-J.; Hu, X.; Yu, J.-H.; Wang, X.-L.; Chapman, T.; Wang, R.-Q. Origin of Late Cretaceous, Enclave-Bearing Granitoids in Southern Tibet: Implications for Magma Recharge and Crustal Thickening. *GSA Bull.* **2023**, *135*, 2391–2406. https://doi.org/10.1130/B36530.1.
49. Elliott, T. Tracers of the Slab. In *Geophysical Monograph Series*; Eiler, J., Ed.; American Geophysical Union: Washington, DC, USA, 2003; Volume 138, pp. 23–45; ISBN 978-0-87590-997-4.
50. Barbarin, B. Mafic Magmatic Enclaves and Mafic Rocks Associated with Some Granitoids of the Central Sierra Nevada Batholith, California: Nature, Origin, and Relations with the Hosts. *Lithos* **2005**, *80*, 155–177. https://doi.org/10.1016/j.lithos.2004.05.010.
51. Clemens, J.D. An Overview of Textural, Compositional and Genetic Relationships between Magmatic Enclaves and Their Host Granitic Rocks. *J. Geol. Soc.* **2026**, *183*, jgs2025-057. https://doi.org/10.1144/jgs2025-057.
52. Vernon, R.H. K-Feldspar Megacrysts in Granites—Phenocrysts, Not Porphyroblasts. *Earth-Sci. Rev.* **1986**, *23*, 1–63. https://doi.org/10.1016/0012-8252(86)90003-6.
53. Vernon, R.H. Crystallization and Hybridism in Microgranitoid Enclave Magmas: Microstructural Evidence. *J. Geophys. Res.* **1990**, *95*, 17849–17859. https://doi.org/10.1029/JB095iB11p17849.
54. Kocak, K.; Zedef, V.; Kansun, G. Magma Mixing/Mingling in the Eocene Horoz (Nigde) Granitoids, Central Southern Turkey: Evidence from Mafic Microgranular Enclaves. *Min. Pet.* **2011**, *103*, 149–167. https://doi.org/10.1007/s00710-011-0165-7.
55. Kumar, S. Schedule of Mafic to Hybrid Magma Injections Into Crystallizing Felsic Magma Chambers and Resultant Geometry of Enclaves in Granites: New Field and Petrographic Observations From Ladakh Batholith, Trans-Himalaya, India. *Front. Earth Sci.* **2020**, *8*, 551097. https://doi.org/10.3389/feart.2020.551097.
56. Cui, X.; Sun, M.; Zhao, G.; Zhang, Y.; Yao, J. Two-Stage Mafic-Felsic Magma Interactions and Related Magma Chamber Processes in the Arc Setting: An Example From the Enclave-Bearing Calc-Alkaline Plutons, Chinese Altai. *Geochem. Geophys. Geosystems* **2021**, *22*, e2021GC009939. https://doi.org/10.1029/2021GC009939.
57. Renna, M.R.; Farina, F.; Ovtcharova, M. Rejuvenation of a Granitic Magma Reservoir by Mafic Injections: Evidence from Zircon U Pb Geochronology, Hf Isotopes and Trace Element Compositions (Porto Complex, Western Corsica). *Lithos* **2025**, *492–493*, 107881. https://doi.org/10.1016/j.lithos.2024.107881.

58. Clemens, J.D.; Stevens, G. What Controls Chemical Variation in Granitic Magmas? *Lithos* **2012**, *134–135*, 317–329. https://doi.org/10.1016/j.lithos.2012.01.001.
59. Barnes, C.G.; Coint, N.; Barnes, M.A.; Chamberlain, K.R.; Cottle, J.M.; Rämö, O.T.; Strickland, A.; Valley, J.W. Open-System Evolution of a Crustal-Scale Magma Column, Klamath Mountains, California. *J. Petrol.* **2021**, *62*, egab065. https://doi.org/10.1093/petrology/egab065.
60. Bonin, B. Do Coeval Mafic and Felsic Magmas in Post-Collisional to within-Plate Regimes Necessarily Imply Two Contrasting, Mantle and Crustal, Sources? A Review. *Lithos* **2004**, *78*, 1–24. https://doi.org/10.1016/j.lithos.2004.04.042.
61. Liesa, M.; Aguilar, C.; Castro, A.; Gisbert, G.; Reche, J.; Muñoz, J.A.; Vilà, M. The Role of Mantle and Crust in the Generation of Calc-Alkaline Variscan Magmatism and Its Tectonic Setting in the Eastern Pyrenees. *Lithos* **2021**, *406–407*, 106541. https://doi.org/10.1016/j.lithos.2021.106541.
62. Karsli, O.; Dokuz, A.; Kandemir, R. Subduction-Related Late Carboniferous to Early Permian Magmatism in the Eastern Pontides, the Camlik and Casurluk Plutons: Insights from Geochemistry, Whole-Rock Sr–Nd and in Situ Zircon Lu–Hf Isotopes, and U–Pb Geochronology. *Lithos* **2016**, *266–267*, 98–114. https://doi.org/10.1016/j.lithos.2016.10.007.
63. Gao, S.; Pei, X.; Pei, L.; Li, Z.; Li, R.; Zhao, S.; Wang, M.; Qin, L.; Wang, X. Origin of Diorites and Coeval Mafic Microgranular Enclaves in the Liuba Region, South Qinling Orogen, Central China: Insights from Petrography, Zircon U-Pb Geochronology and Geochemistry. *Minerals* **2025**, *15*, 77. https://doi.org/10.3390/min15010077.
64. Moyen, J.-F.; Laurent, O.; Chelle-Michou, C.; Couzinié, S.; Vanderhaeghe, O.; Zeh, A.; Villaros, A.; Gardien, V. Collision vs. Subduction-Related Magmatism: Two Contrasting Ways of Granite Formation and Implications for Crustal Growth. *Lithos* **2017**, *277*, 154–177. https://doi.org/10.1016/j.lithos.2016.09.018.
65. Bea, F.; Fershtater, G.; Corretgé, L.G. The Geochemistry of Phosphorus in Granite Rocks and the Effect of Aluminium. *Lithos* **1992**, *29*, 43–56. https://doi.org/10.1016/0024-4937(92)90033-U.
66. Pearce, J.A. Trace Element Characteristics of Lavas from Destructive Plate Boundaries. In *Andesites: Orogenic Andesites and Related Rocks*; Thorpe, R.S., Ed.; John Wiley and Sons: Hoboken, NJ, USA, 1982; pp. 252–548.
67. Pearce, J.A.; Peate, D.W. Tectonic Implications of the Composition of Volcanic ARC Magmas. *Annu. Rev. Earth Planet. Sci.* **1995**, *23*, 251–285. https://doi.org/10.1146/annurev.ea.23.050195.001343.
68. Chappell, B.W.; Bryant, C.J.; Wyborn, D. Peraluminous I-Type Granites. *Lithos* **2012**, *153*, 142–153. https://doi.org/10.1016/j.lithos.2012.07.008.
69. Clemens, J.D.; Stevens, G.; Farina, F. The Enigmatic Sources of I-Type Granites: The Peritectic Connexion. *Lithos* **2011**, *126*, 174–181. https://doi.org/10.1016/j.lithos.2011.07.004.
70. Wang, C.; Song, S.; Zhao, G.; Allen, M.B.; Su, L.; Gao, T.; Wen, T.; Feng, D. Calc-Alkaline Plutons in a Proto-Tethyan Intra-Oceanic Arc (Qilian Orogen, NW China): Implications for the Construction of Arc Crust. *J. Petrol.* **2023**, *64*, egac131. https://doi.org/10.1093/petrology/egac131.
71. Chappell, B.W. Aluminium Saturation in I- and S-Type Granites and the Characterization of Fractionated Haplogranites. *Lithos* **1999**, *46*, 535–551. https://doi.org/10.1016/S0024-4937(98)00086-3.
72. Gao, P.; Zheng, Y.-F.; Zhao, Z.-F. Distinction between S-Type and Peraluminous I-Type Granites: Zircon versus Whole-Rock Geochemistry. *Lithos* **2016**, *258–259*, 77–91. https://doi.org/10.1016/j.lithos.2016.04.019.
73. Zhang, L.; Li, S.; Zhao, Q. A Review of Research on Adakites. *Int. Geol. Rev.* **2021**, *63*, 47–64. https://doi.org/10.1080/00206814.2019.1702592.
74. Martin, H.; Smithies, R.H.; Rapp, R.; Moyen, J.-F.; Champion, D. An Overview of Adakite, Tonalite–Trondhjemite–Granodiorite (TTG), and Sanukitoid: Relationships and Some Implications for Crustal Evolution. *Lithos* **2005**, *79*, 1–24. https://doi.org/10.1016/j.lithos.2004.04.048.
75. Moyen, J.-F. High Sr/Y Rocks Are Not All Adakites. *Geophys. Res. Abstr.* **2010**, *12*, EGU2010–8064.
76. Davidson, J.; Turner, S.; Handley, H.; Macpherson, C.; Dosseto, A. Amphibole "Sponge" in Arc Crust? *Geology* **2007**, *35*, 787. https://doi.org/10.1130/G23637A.1.
77. Plank, T. The Chemical Composition of Subducting Sediments. In *Treatise on Geochemistry*; Elsevier: Amsterdam, The Netherlands, 2014; pp. 607–629; ISBN 978-0-08-098300-4.
78. Turner, S.J.; Langmuir, C.H. An Alternative to the Igneous Crust Fluid + Sediment Melt Paradigm for Arc Lava Geochemistry. *Sci. Adv.* **2024**, *10*, eadg6482. https://doi.org/10.1126/sciadv.adg6482.
79. Galán, G.; Gallastegui, G.; Cuesta, A.; Corretgé, G.; Suárez, O.; González-Menéndez, L. Contrasting Appinites, Vaugnerites and Related Granitoids from the NW Iberian Massif: Insight into Mantle and Crustal Sources. *Eur. J. Mineral.* **2023**, *35*, 845–871. https://doi.org/10.5194/ejm-35-845-2023.

80. Carrigan, C.W.; Mukasa, S.B.; Haydoutov, I.; Kolcheva, K. Age of Variscan Magmatism from the Balkan Sector of the Orogen, Central Bulgaria. *Lithos* **2005**, *82*, 125–147. https://doi.org/10.1016/j.lithos.2004.12.010.
81. Koroneos, A.; Kilias, A.; Avgerinas, A. Hercynian Plutonic Rocks of Voras Mountain, Macedonia, Northern Greece: Their Structure, Petrogenesis, and Tectonic Significance. *Int. Geol. Rev.* **2013**, *55*, 994–1016. https://doi.org/10.1080/00206814.2012.758830.
82. Vavassis, I.; de Bono, A.; Stampfli, G.M. U-Pb and Ar-Ar Geochronological Data from the Pelagonian Basement in Evia (Greece) : Geodynamic Implications for the Evolution of Paleotethys. **2000**, *80*, 21–43. https://doi.org/10.5169/SEALS-60948.
83. Jovanović, D.; Cvetković, V.; Erić, S.; Kostić, B.; Peytcheva, I.; Šarić, K. Variscan Granitoids of the East Serbian Carpatho-Balkanides: New Insight Inferred from U–Pb Zircon Ages and Geochemical Data. *Swiss J. Geosci.* **2019**, *112*, 121–142. https://doi.org/10.1007/s00015-018-0325-4.
84. Huw Davies, J.; Von Blanckenburg, F. Slab Breakoff: A Model of Lithosphere Detachment and Its Test in the Magmatism and Deformation of Collisional Orogens. *Earth Planet. Sci. Lett.* **1995**, *129*, 85–102. https://doi.org/10.1016/0012-821X(94)00237-S.
85. Gómez-Frutos, D.; Castro, A. Mafic Microgranular Enclaves (MMEs) Trace the Origin of Post-Collisional Magmas. *Geology* **2023**, *51*, 743–747. https://doi.org/10.1130/G51248.1.
86. Casini, L.; Cuccuru, S.; Puccini, A.; Oggiano, G.; Rossi, P. Evolution of the Corsica–Sardinia Batholith and late-orogenic shearing of the Variscides. *Tectonophysics* **2015**, *646*, 65–78. https://doi.org/10.1016/j.tecto.2015.01.017.

Disclaimer/Publisher's Note: The statements, opinions and data contained in all publications are solely those of the individual author(s) and contributor(s) and not of MDPI and/or the editor(s). MDPI and/or the editor(s) disclaim responsibility for any injury to people or property resulting from any ideas, methods, instructions or products referred to in the content.